5-5-2017

Tumor Hypoxia Targeted Fluorescence Imaging and Chest-wall-effect Reducing in Ultrasound-guided Diffuse Optical Tomography

Feifei Zhou
University of Connecticut - Storrs, feifei.zhou@uconn.edu

Tumor Hypoxia Targeted Fluorescence Imaging

and

Chest-wall-effect Reducing in Ultrasound-guided Diffuse Optical Tomography

Feifei Zhou, Ph.D.

University of Connecticut, 2017

Abstract

Tumor hypoxia is associated with the malignant progression and tumor responsiveness to therapy. Targeting tumor hypoxia has a profound impact in assessing anti-cancer treatments. Previously we reported the use of 2-nitroimidazole and indocyanine green conjugate (2-nitroimidazole-ICG) to target tumor hypoxia in *in vivo* tumor models. In this study, we evaluated a new generation hypoxia-targeted rigid dye that has a higher fluorescence yield. Results show that it has ~100 nm absorption/emission wavelengths shift and 3-4 times fluorescence quantum yield comparing with 2-nitroimidazole-ICG, as well as more than twice *in vivo* tumor fluorescence intensity. These initial results suggest that the targeted rigid dye may significantly improve *in vivo* tumor hypoxia targeting. Moreover, relationship between hypoxia targeting capability and nitro-linked location was studied. 4-nitroimidazole-piperazine-indocyanine derivative was synthesized by linking the nitro-group at 4^{th} carbon of the imidazole ring. Our *in vivo* hypoxia targeting of 4-nitroimidazole-ICG showed comparable signal to 2-nitroimidazole-ICG, which is consistent with cell and immunohistochemistry results.

We have developed ultrasound (US)-guided diffuse optical tomography (DOT) technique to assist US diagnosis of breast cancer and to predict neoadjuvant chemotherapy response of breast cancer patients. With the US guidance, diffused light measurements were made at the

breast lesion site and the normal contralateral reference site with a handheld hybrid probe, and the data was used to estimate the background tissue optical properties for imaging reconstruction. However, background optical properties were affected by the chest wall underneath the breast tissue. Currently, we have analyzed data from 297 female patients and results have shown statistical significant correlation between fitted optical properties (μ_a and μ_s') and the chest wall depth detected by a boundary detection algorithm applied to co-registered US images ($r > 0.27$, $p < 1.0 \times 10^{-4}$). After subtracting background μ_a at each wavelength, the difference of computed total hemoglobin (tHb) between malignant and benign lesion groups has improved. Receiver operating characteristic (ROC) curve analysis shows significant improvement for predicting early malignant lesion diagnosis after subtraction. For early stage malignant lesions, the area-under-the ROC curve (AUC) has improved from 88.5% to 91.5%. For all malignant lesions, the AUC has improved from 85.3% to 88.1%.

Tumor Hypoxia Targeted Fluorescence Imaging and Chest-wall-effect Reducing in Ultrasound-guided Diffuse Optical Tomography

Feifei Zhou

B.S. Huazhong University of Sci. & Tech. , Wuhan, China, **[2006]**

M.S. University of California in Davis, Davis, **[2012]**

A Dissertation

Submitted in Partial Fulfillment of the

Requirements for the Degree of

Doctor of Philosophy

at the

University of Connecticut

[2017]

APPROVAL PAGE

Doctor of Philosophy Dissertation

Tumor Hypoxia Targeted Fluorescence Imaging and Chest-wall-effect Reducing in Ultrasound-guided Diffuse Optical Tomography

Presented by

Feifei Zhou, M.S.

Major Advisor

_____

Quing Zhu

Co-major Advisor

_____

Rajeev Bansal

Associate Advisor

_____

Michael Smith

Associate Advisor

_____

Xiuling Lu

Associate Advisor

_____

Guoan Zheng

University of Connecticut
[2017]

Acknowledgements

I have been lived in UConn, Storrs, CT for four years and four months. For me this is like another journey after the previous one. During this studying period, I am so glad to have all people: my adviser, teachers, lab mates, students, friends and family members, to be with me in experiencing the rules and rewards, up and falls in life.

I am grateful to have met Dr. Zhu, my adviser and mentor, in my studying life in the United States. She opens a new window to me and bestowed another chance upon exploiting myself in the academic world. Whether I am gifted or not, she is always trying to search for the possibility that I could be flourish in any of the projects I could do. Teaching from her is so alive that is spread into every of the daily events, and little by little: So many times when I was doubting the continuation of my project, she was insisting and proposing ways of solving the problems. So much time and efforts were put in doing a solid work for the paper presentation. Rounds of clinical sampling trips I went with her were knitted with discussions on the problem solving and future improvement. The conferences trips were also promoted her support in better presenting our works and making greater networks for our future career life. No matter how many more life journeys I will be in later, these precious memories should be printed in my mind and guide me through any confusing and discouraging circumstances.

I would also like to thank Dr. Smith, Micheal, Dr. Lu, Xiuling, Dr. Bansal, Rajeev, Dr. Bruckner, Christian, and Dr. Zheng, Guoan, for their helps either in providing me with materials for experiment, or letting me do experiments in their labs, or providing me with suggestions or comments in my studying. These gave me opportunities in looking my projects and problems from another perspective and also opportunities to exchange my ideas with students from their labs.

My acknowledgement also given to Saeid Zanganeh, Akram Abuteen, Patrick Kumavor, Hamed Vavadi, Mohsen Erfanzadeh, Atahar Mostafa, Guangqiang Yuan, Murad Althobaiti, Jinglong Li, Sreyankar Nandy, Hassan Salehi, Shihab Uddin, Hai Li, Tianheng Wang, my lab mates and friends. Special thanks to Mohsen Erfanzadeh for helping with SDS-PAGE gel imaging, and to Atahar Mostafa for developing the chest wall depth algorithm. I am lucky to have a lot of shared memories with them during these years. Every one of us has unique personalities and is coming from different cultures and background, but my closely collaborative working experiences with most of them made me seeing my shortcomings in a clearer way. Although there is not always a good feeling at the beginning, later experiences worked significantly in pruning my mind and opening my eyes. The feelings that I am able to do something and am needed to some extent in a group is so helpful in promoting my daily works. A same feeling was felt during my TA working experiences. Initially I just wanted to practice my speaking English, which is a problem for most students coming from China. I was endowed with a lab TA position in the large Circuit class, and saw my initial intention fulfilled in a fast way. I felt I was teaching and studying at same pace, and by working with the students, other TAs and professors it really enriched my life and gave me some ideas in better presenting our thoughts in communication.

Last but not the least, I would like to thank my friends who are always there for me, for their support, and my parents and husband. Carol, Joyce, Yanping, Wanqing, Tong, Fengyu, Xin, Donghui…, who fills my life with joy and peace in UConn and who I also have learnt gradually from. Deepest thanks to my parents and my husband, who have been giving unconditional love and continuous support to me.

Table of Contents

List of figures

List of tables

Abbreviations

Al_2O_3 aluminum oxide

API Asian-Pacific Islander

AUC area under the ROC curve

BSA bovine serum albumin

CT computed tomography

CW continuous wave

Cy5 Cyanine Dyes 5

DOS diffuse optical spectroscopy

DOT diffuse optical tomography

ECM extracellular matrix

FA fibroadenoma

FC fibrocystic tissue

FD frequency domain

FITC Fluorescein isothiocyanate

FN fat necrosis

FPR false positive rate

Hb deoxygenated-hemoglobin

HbO_2 oxygenated-hemoglobin

HER2 human epidermal growth factor receptor 2

HR hormone receptor

ICG indocyanine green

IHC immunohistochemistry

LN lymph nod

MRI magnetic resonance imaging

NIR near infrared

NPV negative predictive value

PET positron emitting tomography

PPV positive predictive value

Prolif. proliferative

PSF point spread function

ROC receiver operative characteristics

RTV Room Temperature Vulcanization silicone

SDS-PAGE sodium dodecyl sulfate polyacrylamide gel electrophoresis

SiO_2 silicon dioxide

SNR signal to noise ratio

SO_2 oxygen saturation

STD standard deviation

tHb total hemoglobin

TiO_2 titanium dioxide

TPR true positive rate

TR time-resolve

Chapter 1 Introduction

Minimal or non-invasive cancer detection and diagnosis using optical techniques in the near infrared (NIR) range have been extensively studied in the biomedical field. Compared with conventional diagnosing techniques such as the magnetic resonance imaging (MRI) and computed tomography (CT), optical imaging of early stage tumors is quite promising due to its low-cost, high sensitivity and non-radiative characteristics. As biological tissues generally have high absorption and scattering optical coefficient which cause a fast attenuation of light in the VIS-UV range and therefore impede the optical detection of tumor embedded under skin, NIR light is more used for these studies. And the breast, prostate and brain tumors are some major subjects of these studies due to their special physical structure appealable for the application of optical imaging.

There are various of methods in terms of *in vivo* tumor diagnosis using optical techniques. Fluorescence imaging and diffuse optical spectroscopy or tomography (DOS or DOT) are two methods among them. For the fluorescence tumor imaging, where the signal is generally low compared with the excitation, and the fluorescence usually comes from more than one fluorophore, a fluorescent probe that specifically target the tumor region can significantly increase the signal to noise ratio (SNR), therefore improves the sensitivity and accuracy of tumor detection. In the area of diffuse optical spectroscopy or tomography, which is based on the diffuse theories of light propagation in tissue, many different systems have been developed and proved to be useful for tumor detection, as it will be discussed later in Chapter 4. Currently, methods in either algorithm, hardware or data analysis that improve sensitivity, stability and accuracy are of most interest to investigate. This thesis is mainly aimed to discuss and report different methods we used for improving these two modalities in breast tumor diagnosis,

testing methods of these improvements, and the statistical analysis of the improvements with either animal or clinical data.

The structure of this thesis is stated as below: **Chapter 1** gives a brief introduction on the background of each studies that are discussed later. The topics include: breast cancer status, the optical screening of breast cancer, some basic theories in tissue optics, the main cancer biomarkers under investigation (including the total hemoglobin (tHb), oxygen saturation (SO_2) and tumor hypoxia), and then the phantom that mimics breast tissue used for systems calibration. **Chapter 2** describes the novel fluorescence dyes developed by our collaborator Dr. Smith's lab, for tumor hypoxia labeling. It focuses on the animal tumor studies and tests on both rigid dye and piperazine-4-nitroimidazole-ICG dye. For a deeper understanding of the hypoxia targeting properties of these dyes, **Chapter 3** introduces a biotin dye study with both *in vivo* experiment and excised tumor tissues. **Chapter 4** reviews the current existing diffuse optical systems used for breast cancer diagnosis, their principles and reported diagnostic results. By comparing our DOT system with the ones developed by other groups, we proposed a background subtracting method for reducing a problem specifically exists in our DOT system or any DOT systems using similar method to ours. Later, a solid statistical analysis of the diagnostic improvement using this method with 297 patients' data was discussed. **Chapter 5** describes a phantom study using hemoglobin for the DOT system calibration and imaging test. **Chapter 6** is a summary and proposes some future works at the end.

1.1 Breast cancer

According to a recent annual cancer status report based on national cancer data through 1975-2011, breast cancer is the most common cancer for women by a wide margin among all racial and ethnic groups in the United States, and is one of the three top leading causes of cancer

death for women (the other two are lung and colorectal cancers) [1]. Understanding the cause of breast cancer is one of the most important purposes of breast cancer study.

The reason for cause of breast cancer at the early stage can be a comprehensive combination of multiple factors. A major opinion relates breast cancer to the hormone receptor expression (HR+/-) and human epidermal growth factor receptor 2 (HER2+/-), which are proteins associated with picking up signals that tells cells to grow [1]. According to the report, the breast cancer can be categorized as four subtypes: Lumina A (HR+/HER2-), Lumina B (HR+/HER2+), HER2-enriched (HR-/HER2+) and triple-negative (HR-/HER2-, also referred as basal-like). Additional analysis also showed that the incidence of HR+ breast cancer is much higher than the other subtypes, while it is least likely to develop into an invasive breast cancer in later stages. Its development is more related with the reproductive factors, including the breastfeeding, number of children and age of first birth, *etc*. Moreover, the basal-like triple-negative breast cancer is more racial and ethnic related and is more likely to develop into an invasive breast cancer [1].

1.2 Optical screening of breast cancer

The significance of optical screening in early stage breast cancer has been implied by the statistical report that the death rates due to breast cancer among females during 5 years span (2007-2011) decreased by 1.9% compared with the 10 years span (2002-2011) data with significant *p-values*, while the incidence of breast cancer remains stable during that time range [1]. Moreover, the ranking of mammography use is highest in whites, blacks, API (Asian-Pacific Islander), and lowest in Hispanics, respectively. It matches the racial/ethnic rankings for HR+/HER2- breast cancer incidence rates, meaning more cancers of this type were discovered. In addition, HR+/HER2- cancer (which ranges the highest cause of breast cancer)

is high in low poverty areas, implying that disparities in access to health services and subsequently utilization of cancer screening may contribute to the difference.

In most of the developed world, screening women for cancer annually for preventing disease has become the 'standard of care' for women over the age of 50 [2]. However, an important challenge remains to reduce the over-diagnosis and not true excess in disease occurrence. And still there are populations where this screening program does not work well, including: highly ratio-dense breast tissue, known higher risk due to genetic factors, complex breast tissue due to previous surgery, and younger women who are within the age range where annual screening is recommended.

To sum up, optical screening is important in discovering the incidence of early stage breast cancer, and improving the cure rate of HR+ type breast cancers. And it is also indicated by the report that there are spaces for improving the optical screening technique and implementation.

1.3 Tissue-light interaction

For optical screening of breast, light passing through the tissue carries information about optical properties of the tissue. The beam of light can be viewed as many photons incident from the same location with similar direction. When a photon propagates in tissue, it undergoes millions of events of scattering, and after those it may disappear due to the absorption of tissue, or be reflected or transmitted through the tissue medium. The absorption and scattering coefficients (μ_a and μ_s) characterize the probability of the occurrence of each event. According to tissue optics, μ_a is associated with absorbers/chromophores in tissue, including the melanin in skin, hemoglobin in blood, and some other molecules such as the fluorophore. And μ_s is associated with small particles including the cell membrane, mitochondria, and collagen fibers in the extracellular matrix (ECM).

Since μ_a and μ_s are light wavelength dependent, it always has the advantage in using the NIR light with wavelength ranging 700-1000 nm for optical screening of tissues. For the chromophores and water in tissue, there is an absorption valley for light 600-1300 nm (the optical window, as shown in Fig. 1.1). In this range, the excitation light is absorbed less and penetrates deeper than those at shorter or longer wavelengths, meaning the reflective or transmitted signal carries information of tissue from deeper location or with larger thickness. Although the penetration depth of NIR light in tissue varies by the tissue type, for general breast tissue, this falls in several centimeters scale.

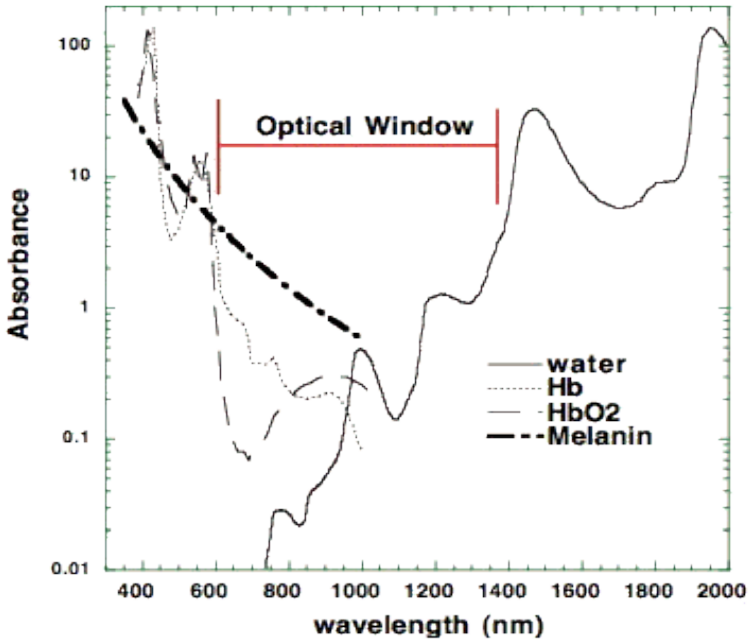

Figure 1.1. Optical absorbing spectra of tissue and optical window [3]

1.4 Hemoglobin content and oxygen saturation

According to part 1.2, it was reported by many studies that the hemoglobin content (including oxygenated hemoglobin, HbO_2 and de-oxygenized hemoglobin, Hb) and oxygen saturation (SO_2, defined by the ratio of HbO_2 over total hemoglobin) are closely related with tumor

development. The hemoglobin generally increases due to angiogenesis for providing more nutrition and oxygen to breast tumor for keeping the rapid growing speed. But the SO_2 changes in a complicated way either due to the irregular vasculature in tumor or fast consumption of oxygen by tumor cells. Part of the tumor tissue shows extremely low SO_2 when tumor develops to the later stages. This poses problems to therapeutic or radiative treatment as drugs are delivered to tumor through blood circulation, or radiative agents' effects depend largely on the oxygen concentration. The relationship between total hemoglobin/SO_2 and age, menstrual cycle effects, menopausal status, pregnancy number, breast density, body mass index (BMI), skin color, are also under intensive studies. And the study subjects are not limited to the lesion breast, but also the normal contralateral breast.

In order to estimate the concentrations of hemoglobin, measurements of tissue absorptions at more than two wavelengths are needed. More wavelengths measurements lead to more solid hemoglobin concentrations solution. Our DOT system used four wavelengths light ranging from 740-830 nm as the signal, and the four measured absorption coefficients are to be plugged in the equation below to determine the concentration of hemoglobin by least square solution [4].

$$\begin{bmatrix} \mu_{a\lambda 1} \\ \mu_{a\lambda 2} \\ \mu_{a\lambda 3} \\ \mu_{a\lambda 4} \end{bmatrix} = 2.303 \begin{bmatrix} \varepsilon_{HbO_2\lambda 1} & \varepsilon_{Hb\lambda 1} \\ \varepsilon_{HbO_2\lambda 2} & \varepsilon_{Hb\lambda 2} \\ \varepsilon_{HbO_2\lambda 3} & \varepsilon_{Hb\lambda 3} \\ \varepsilon_{HbO_2\lambda 4} & \varepsilon_{Hb\lambda 4} \end{bmatrix} \begin{bmatrix} c_{HbO_2} \\ c_{Hb} \end{bmatrix} \tag{1.1}$$

Where the ε is the extinction coefficients for HbO_2 and Hb at specific wavelengths, as can be found in the known spectra (Fig. 1.2) [4].

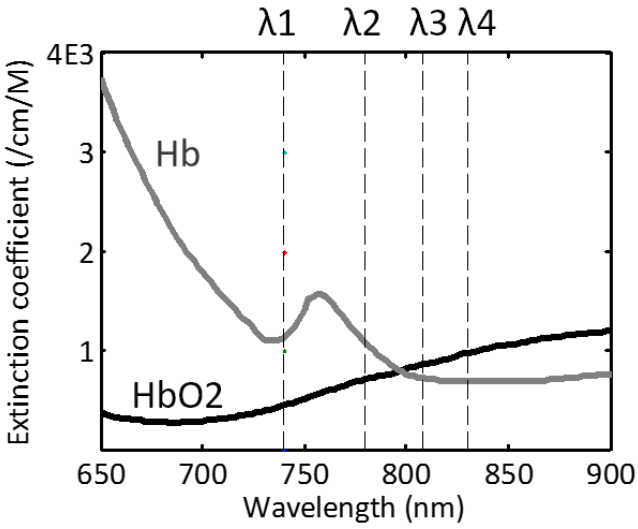

Figure 1.2. Hemoglobin extinction coefficients

1.5 Tumor hypoxia and our studied dyes

Tumor hypoxia mainly appears as a structural or functional misbalance between the tumor micro-environmental oxygen supply and consumption, and is associated with the rapid progression of malignant tumors [5-8]. Tumor hypoxia is an important target in the assessment and prediction of therapy, as it is known to cause the aggressive phenotype and increased resistance to therapy [9, 10]. Positron emission tomography (PET) is an established method for imaging hypoxia noninvasively [11]. Imidazole compounds are widely used to prepare PET radionuclides, and it is known that 2-nitroimidazoles show an affinity for hypoxic cells, with the highest electron affinities of this class of compounds [12-16]. Problems associated with PET, including the requirement that radioactive tracer must be administered to patients by injection, as well as the high system cost, have spurred the development of alternative tumor hypoxia imaging techniques.

Indocyanine green (ICG) is the only FDA approved fluorescence imaging agent for patient use, but its application is hindered by problems such as low quantum yield and quick loss of fluorescence after binding to protein in circulating blood [17-19]. The 2-nitroimidazole and ICG conjugate using piperazine linker (piperazine-2-nitroimidazole-ICG) was previously reported by our our and Dr. Smith's lab in UConn department of Chemistry to improve tumor hypoxia targeting as compared with the first generation 2-nitroimidazole ICG conjugate using ethanolamine linker (ethanolamine-2-nitroimidazole-ICG) [20]. Later, based on the hypothesis that molecules with more planar and rigid structures have a higher fluorescence yield as they could release less absorbed energy through molecular vibration or collision [21, 22], Dr. smith's lab have developed the third generation of 2-nitroimidazole ICG conjugate. This conjugate has 2 carbons less in the polyene linker, and is studied and referred as the hypoxia-targeted rigid dye in the following text [23]. The bis-carboxylic acid referred as non-targeted rigid dye was also tested for comparison with hypoxia-targeted rigid dye.

1.6 Optical and ultrasound phantoms

Phantoms are the manufactured tissue-simulating objects for purpose of mimicking the properties of human or animal tissues [24]. They generally serve as the standard measuring target for calibrating new systems and routinely monitoring of existing systems, especially for the optical and ultrasonic ones. They are usually generated with the matrix, absorber(s), scatterer(s) and/or fluorophore(s). Aqueous suspension or solid phantoms made with agar or silicon rubber can be used as the matrix for holding the scatterers, absorbers and/or fluorophores. Ink, blood or molecular dyes are generally used as the absorbers. Intralipid (used for aqueous suspension), titanium dioxide (TiO_2), aluminum oxide (Al_2O_3) and microspheres

can be used as the scatterers [24]. The manufacturing procedures varies, however, eventual optical properties are expected to be as close as possible to the study tissues [24].

One method of making a phantom is to directly use the hemoglobin. Hemoglobin is the main absorber in red blood cells. Many companies provide products of purified hemoglobin in different forms. It can be filled arbitrary concentration in a clear container or mixed in solid mixture to mimic the absorbing target (such as the diseased part) in tissue. Although it's hard to make arbitrary SO_2, it is possible to make hemoglobin phantom with SO_2 equals close to 0 and 100%, under extreme conditions. In the study described in this thesis, we added $Na_2S_2O_4$ powder to oxygenated-hemoglobin solution to make it de-oxygenated for system calibrations.

Chapter 2 Tumor hypoxia targeted fluorescence dyes

2.1 Introduction

In the previous work, Nrusingh *et al.* have demonstrated a noninvasive method for *in vivo* imaging of hypoxic tumors [25]. This method is based on fluorescence NIR imaging of dyes in hypoxic tumors, after injection of a nitroimidazole-indocyanine dicarboxylic acid conjugate, henceforth referred to as a dye-conjugate. In that work, dicarboxylic acid **2** was used as the untargeted dye rather than **1**, and 2-nitroimidazole was linked to the dye using ethanolamine [20, 25] or piperazine [26] linkers as shown in Fig 2.1, which are referred as the hypoxia targeting ethanolamine-dye conjugate **3** and a piperazine-dye conjugate **4**, respectively.

The first-generation dye conjugate (**3**) was shown to be a successful candidate for non-invasive tumor hypoxia mapping using a near-infrared fluorescence imaging technique [20]. The fluorescence signals were measured to be two-fold higher at the tumor site, relative to the untargeted dye **2** [27]. Immunohistochemistry stains for tumor hypoxia, using Hypoxyprobe™-1, showed that hypoxic areas in the tumor correlated with the presence of dye-conjugate **3**. Furthermore, it was showed that **3** could be detected in the tumor for 5-7 h, post-injection. The ester linkage in **3** was viewed as too labile and in an effort to improve *in vivo* efficacy the ethanolamine moiety was replaced with a more robust piperazine moiety, generating the second-generation dye conjugate **4** [26]. *In vivo* targeting experiments in mice with **4** showed a two-fold higher fluorescence in hypoxic tumors relative to **3**, within three h of injection, and the florescence was 1.6-1.7 times higher beyond three h [26].

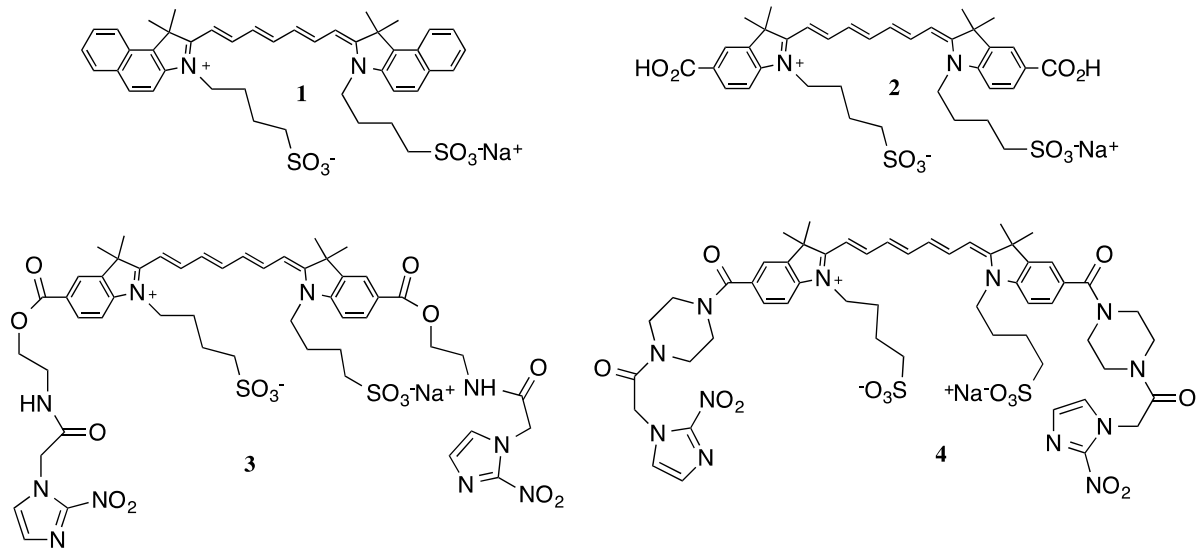

*Figure 2.1. Indocyanine dyes (**1**, **2**) and first and second-generation dye conjugates (**3** and **4**)*

Further efforts have focused on the improve of the fluorescent yield of the dye. It is known that molecules with more planar and rigid structures have a higher fluorescence yield as they release less absorbed energy via molecular vibration or collision [21, 22]. Based on this hypothesis, a ring was introduced into the polyene unit of **2** by Dr. Smith's lab. It was found to led to a lower *in vitro* fluorescent yield, but shortening the polyene chain by two carbon atoms (**8**) led to significant enhancement in the *in vitro* fluorescence [23]. After that, a third generation 2-nitroimidazole ICG conjugate (**12**) was synthesized from new dye **8**, which is the hypoxia-targeted rigid dye, as shown in Fig. 2.2. The bis(carboxylic acids) **2** and **8** are referred to as non-targeted dyes because they do not have the nitroimidazole moiety associated with targeting tumor hypoxia. The goal of this study is to quantify the *in vivo* hypoxia targeting capability of **12** relative to the non-targeted dyes as well as relative to **4**, using a murine tumor model. A direct comparison of the *in vivo* performance of the rigid dye-conjugate **12** with the second-generation hypoxia-targeting dye (**4**) showed greatly improved imaging for **12**. The

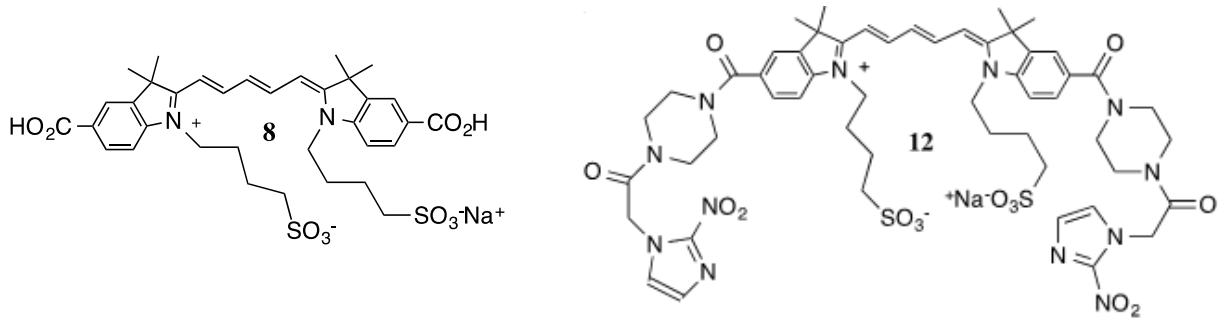

*Figure 2.2. Molecular structure of non-targeted rigid dye **8** and targeted rigid dye **12**.*

bio-distribution of each dye in different organs was also evaluated and compared with the dye uptake in the tumor.

In another study, the relationship between hypoxia targeting capability and the nitroimidazole linked location was also studied [28, 29]. Although both 2-nitroimidazoles and 4-nitroimdazole derivatives have been studied as radiopharmaceuticals in hypoxia, 2-nitroimidazoles are most commonly used as hypoxia labeling markers since it has a higher electron affinity and a higher reduction potential than either 4-nitroimidazole or 5-nitroimidazole [30]. In addition, the 4-nitroimidazole compounds were shown to be toxic [31]. Therefore, the initial works focused on the known affinity of 2-nidtroimidazole compounds for tumor hypoxia as a molecular probe. However, the cost of 2-nitroimidazole is nearly prohibitive in synthesizing the 2-nitroimidazole dye-conjugates. Based on price considerations alone, the preparation of a 4-nitroimidazole dye-conjugate was a worthy goal. Despite the concerns about the toxicity of 4-nitroimidazole derivatives, previous work by other groups showed that 4-nitroimidazole complexes used for imaging tumor hypoxia was feasible [32].

In this work, we report at first on the performance of hypoxia targeted rigid dye in comparing with the second generation untargeted (**2**) and targeted ICG dye conjugate (**4**) [33]. After that, we also report the performance of the piperazine-4-nitroimidazole-ICG derivative

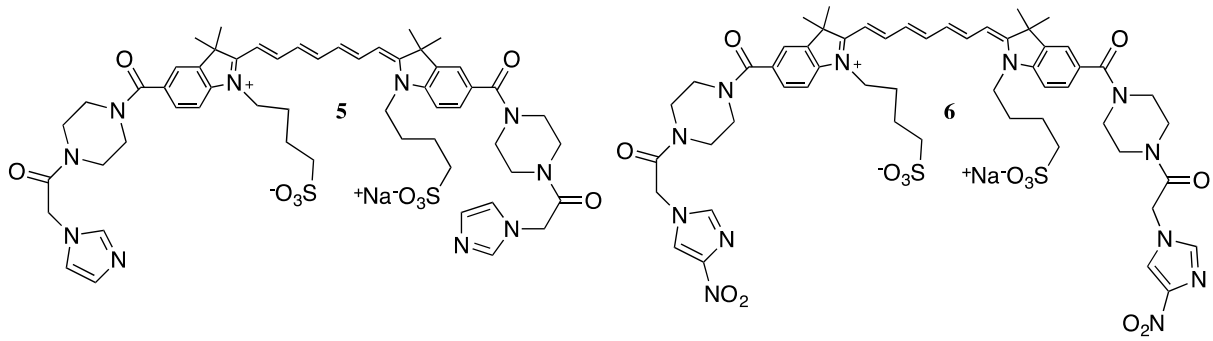

*Figure 2.3. Molecule structure of imidazole ICG (**5**) and 4-nitroimidazole ICG dye-conjugate (**6**)*

6, using the unsubstituted imidazole derivative **5** as a reference (Fig. 2.3). A comparison of the hypoxia targeting performance of **6** and **5** in balb/c tumor-bearing female mice, with the previously tested piperazine-2-nitroimidazole-ICG dye-conjugate (**4**), is also discussed. We used various techniques to validate our findings in the *in vivo* experiments.

2.2 Materials and Methods

2.2.1 Measurement of quantum yield

In order to measure the quantum yield of hypoxia-targeted rigid dye **12** and non-targeted rigid dye **8,** we followed the procedures described in the reference [34]. Any of these four unknown samples is measured against a fluorescence standard, Indocyanine green (ICG) from Sigma-Aldrich with a known quantum yield Φ_f =0.012 [35] with Varian Cary® 50 UV-Vis Spectrophotometer and Varian Cary® Eclipse Fluorescence Spectrophotometer. The fluorescence quantum yield is then calculated according to eq. 2.1, by taking into account the absorbance through the absorption factor $f_x(\lambda_{ex})$ and the fluorescence through the integral of fluorescence $F^x(\lambda_{em})$ at specific excitation wavelength λ_{ex} and a range of collection wavelength band λ_{em}.

$$\Phi_f^i = \Phi_f^s \frac{f_s(\lambda_{ex})}{f_i(\lambda_{ex})} \frac{\int_{\lambda_{em}} F^i(\lambda_{em})}{\int_{\lambda_{em}} F^s(\lambda_{em})} \quad (2.1)$$

Here both standard (*s*) and unknown dye (*i*) were measured in 9.25% sucrose, thus compared with the reference, the difference of refractive indices between standard and unknown dye can be ignored. The excitation/collection wavelengths are shown in Fig. 2.4.

2.2.2 Murine tumor model and imaging

6-8 weeks old balb/c mice with body weight around 20g were used in this study and transplanted with 4T1 tumor cells. The experiments were performed when the tumor size had attained a diameter of 5 mm or greater, 10-15 days post-inoculation. Mice with a tumor bared on the top of their right legs were imaged with an IVIS® Lumina II Imaging System (Caliper Life Sciences, Hopkinton, MA) [36].

Mice were separated into four groups with similar average tumor size. Each group of mice was injected, via retroorbital injection, with 100 µl of either biscarboxylic acid ICG (**2**), piperazine-2-nitroimidazole-ICG (**4**), non-targeted rigid dye (**8**), or hypoxia-targeted rigid dye (**12**) at a concentration of 25 µM.

Imaging the tumors began 1 minute post-injection and were repeated at 5 min, 15 min, 30 min, 1, 2, 3, 4, 5, 6, 7, 8, 9, 10, 24 and 48 h. In all cases, the *in vivo* fluorescence intensity was quantified. After 48 h, the tumor tissue was excised from each sacrificed mouse, and immediately frozen in the liquid nitrogen. After acquiring florescence images, the tissues were stored in the -80 °C freezer for later histology processing.

2.2.3 Immunohistochemistry

To visualize the hypoxic area in the tumor samples by immunohistochemistry (IHC), the Hypoxyprobe™1 plus kit, which contains the 2-nitroimidazole derivative pimonidazole hydrochloride [1-(2-nitro-1*H*-imidazol-1-yl)-3-(piperidin-1-yl)propan-2-ol] was purchased

from HPI, Inc. (Burlington, Massachusetts, USA). A total of 60 mg of pimonidazole hydrochloride per kg body weight, diluted in 0.9% saline solution was injected intravenously into mice 30-45 minutes before sacrificing. Immediately after the animals were euthanized, the tumor specimens were collected and flash-frozen in the liquid nitrogen, and subsequently sectioned into 16 μm sections on a Leica CM 3050S cryotome (Leica, Nussloch, Germany). The prepared tumor sections (sample number: **8** for hypoxia-targeted rigid dye, **12** for non-targeted rigid dye) were stored in -80 °C before staining. After thawing, the sections were fixed in cold acetone for 10 minutes, and later rinsed and incubated overnight at 4 °C with FITC-Mab1 diluted 1:20 in PBS containing 0.1% bovine serum albumin and 0.1% Tween 20.

The hypoxic areas were visible with FITC attaching to pimonidazole hydrochloride under the fluorescence microscope (Zeiss Axio M2, Pennsylvania, USA). In order to analyze the targeting property of **12** in tumor, fluorescence images are acquired simultaneously with filter sets for channel 1- Cy5 and channel 2- FITC. The absorption and emission peaks of Cy5 (650/670 nm respectively) are overlapped with that of **12** and **8**. Digital images of the whole tissue slices were scanned and acquired with 2.5× and 10× objective magnifications. For 10× magnification, the exposure time is used as 1200 ms for channel 1 and 250 ms for channel 2. Obtained digital images were transferred to ImageJ software, delineated with the boundaries of hypoxic areas, split by channels for separate analysis. Each image is later imported to Matlab, converted into a binary image with a threshold of 12% of the labelled tissue area, and used for computing the correlation of the labelled areas between pimonidazole hydrochloride and the rigid dye (**12** or **8**).

For the 4-nitroimidazole dye study, comparison was also made with the labeled areas on tumor tissue sections stained with the Hypoxyprobe™-1 probe and our dyes (dye **4**, **5** and **6**).

As the excitation and collection wavelengths for dye **4**, **5** and **6** are in the 700-800 nm range and cannot be imaged with regular fluorescence microscope, we used the Odyssey Infrared imaging system (Li-Cor Bioscience, Nebraska) to image the residues of our dyes. The system provides two excitation wavelengths (660 nm and 780 nm) and resolution ranging 21 to 339 μm. For this study, we chose the 780 nm excitation channel and scanning resolution at 21 μm. Other parameters were set as: focus offset, 0.5mm; intensity, 5.0; quality, high. After the images were acquired, the average of integrated intensity was computed and a comparison was made among dye **4**, **5** and **6**.

2.2.4 Hypoxia versus normoxia cell experiments (for the 4-nitroimidazole dye study)

Hypoxia-dependent targeting of the dye was assessed using 4T1 breast cancer cells. Twelve dishes (T7425-2, 60 x 15 mm, BD Falcon, NJ, USA), with approximately 1 million 4T1 cells each were evaluated. One group of six dishes was exposed to hypoxic conditions (5% CO_2, 1% O_2, 94% N2, 37°C) by passing the gas mixture (5 psi at room temperature) into a hypoxic chamber (Billups-Rothenberg Inc, CA, USA) for 10 min. The gas mixture was provided by Airgas East (Cheshire, Connecticut). The chamber was then sealed and incubated for 15 h. The second group of six dishes was incubated under normoxic conditions (5% CO_2, 95% O_2, 37°C) for the same period. Two dishes of each groups were treated with 3 ml of either **6**, **4**, or **5** at 15 μM. Then the hypoxic group was put back into the hypoxic chamber and re-incubated both for 9 h. The medium was then removed and dishes were rinsed with PBS and immediately taken for imaging using the Lumina II Imaging System.

2.3 Results

2.3.1 *In vitro* measurements of rigid dyes

The optical properties of **12** were measured and the normalized spectra are displayed in Fig. 2.4. It shows that in measuring the quantum yield with the standard dye of ICG from Sigma-Aldrich, the excitation was performed at 640 nm, as labeled with arrows. The fluorescence was collected from 650-900 nm for all dyes. Six concentrations of each dye were measured for the calculation of quantum yield. All dyes are measured with spectrometer gain set at medium and the measurements are performed in 9.25% sucrose. The spectra of non-targeted rigid dye **8** is similar to that of **12**. The spectra peak wavelengths of biscarboxylic acid ICG **2** and piperazine-2-nitroimidazole-ICG **4** are also similar, as can be referred to the past report [26]. The absorption maximum for **12** was at 657 nm and the emission maximum was at 670 nm, a shift of around 100 nm and 110 nm for absorption and emission, respectively, when compared with **4**. The other measured optical properties for non-targeted rigid dye **8** and hypoxia-targeted rigid dye **12** in 9.25% sucrose solvent are shown in Table 2.1.

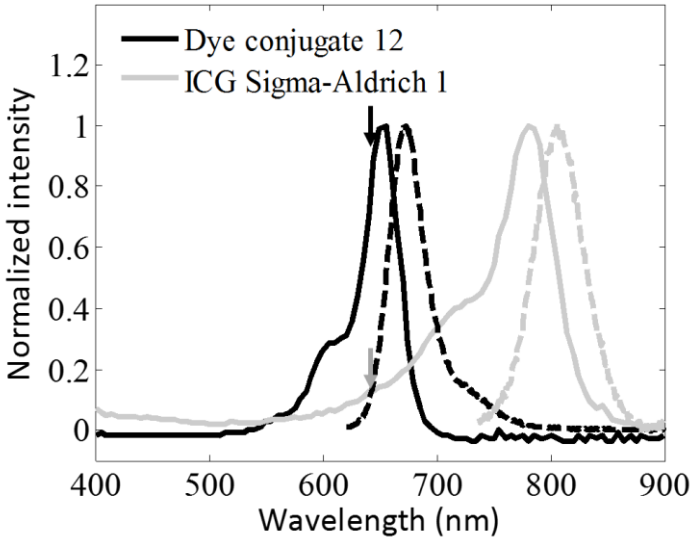

*Figure 2.4. Normalized absorption (solid curves) and fluorescence (dash curves) spectra of hypoxia-targeted rigid dye **12** (black) and ICG from Sigma-Aldrich **1** (gray).*

Table 2.1. The optical properties of rigid dyes in 9.25% sucrose solution

Compound	$\lambda_{abs}^{max}(nm)$	$\lambda_{ems}^{max}(nm)$	Extinction coefficient ε ($M^{-1}cm^{-1}$)	Quantum yield (Φ)
Non-targeted rigid dye 8	657	671	261,971	0.403
Hypoxia-targeted rigid dye 12	657	669	268,006	0.467

2.3.2 The *in vivo* distribution of the Dye-Conjugate as a function of time

Fig. 2.5 shows a typical set of fluorescent images obtained by IVIS Lumina II Imaging System over a 48-hour period for a mouse injected with 100 µl of biscarboxylic acid ICG **2** (a), piperazine-2-nitroimidazole-ICG **4** (b), non-targeted rigid dye **8** (c) and hypoxia-targeted rigid dye **12** (d) at 25 µM concentration. The first row shows fluorescent images obtained by IVIS Lumina II Imaging System using a 710±15 nm/810-875 nm excitation/collection filter pair over a 48 h period for individual mouse injected with 100 µl of (a) biscarboxylic acid ICG **2**; (b) piperazine-2-nitroimidazole-ICG **4** at 25 µM. The second row shows fluorescent images using a 640±15 nm/695-770 nm excitation/collection filter pair over a 48 h period for individual mouse injected with 100 µl of (c) non-targeted rigid dye **8** and (d) targeted rigid dye **12** at 25 µM. The tumor area for each case was labelled with red circles when the tumor

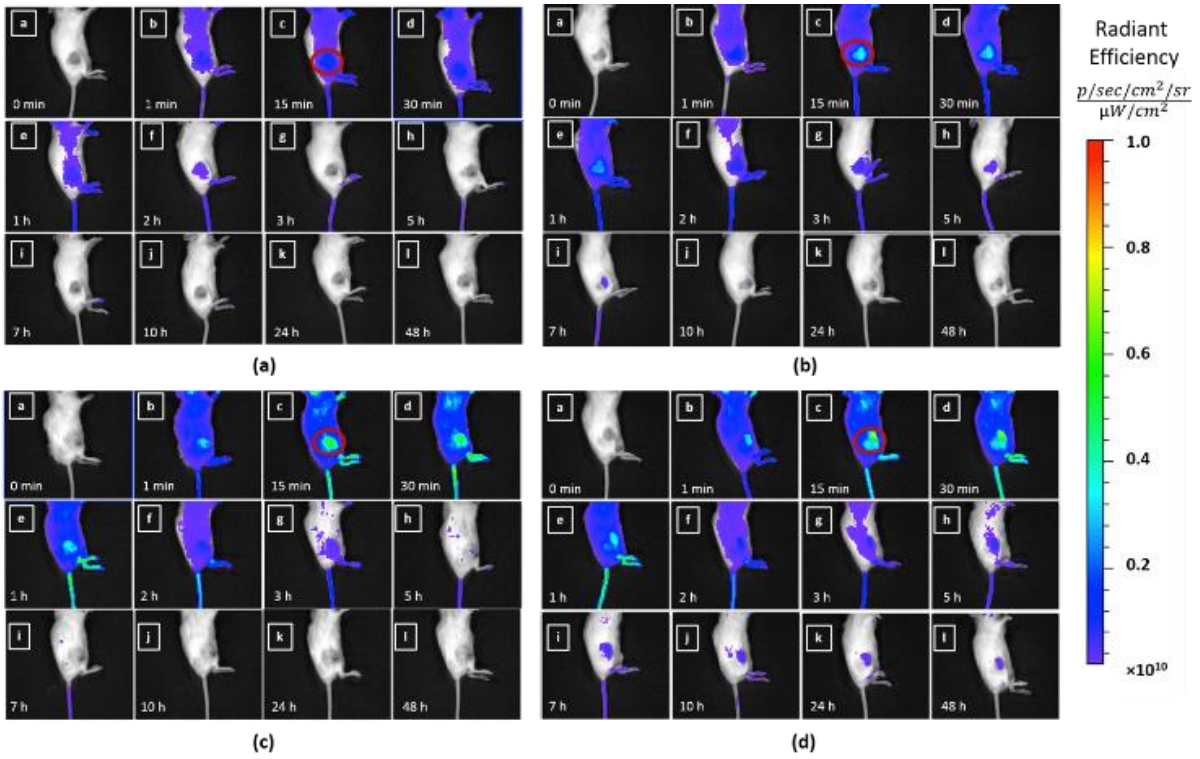

*Figure 2.5. Typical sets of fluorescent images as a function of time injected with dye **2** (a), **4** (b), **8** (c) and **12** (d) at 25 μM.*

fluorescence intensity reaches to the peak at around 15 min post-injection. All dyes were accumulated in and cleared from the tumor area with visible and different washout rates, reflecting tracer-specific uptake mechanisms. The improvement on the fluorescence intensity of dye **12** accumulated in the tumor region and longer washout time compared with the other dyes are visible from Fig. 2.5.

2.3.3 Dye washout characteristics

The washout curves of each dye in tumor area were averaged at each observation point, and the bar plot with STD for washout period is shown in Fig. 2.6. All tracers were injected at 25 μM concentration. It is shown that for **12** the fluorescence intensity reached an average maximum of 8.0×10^9 (Radiant efficiency, unit: p/sec/cm^2/sr/(μW/cm^2)) in 5-15 min post-injection and the signal remained above detection level (2×10^8, decided by background

fluorescence) in 48 h. For **8**, the fluorescence reached an average maximum of 7.0×10^9 in 5-15 min post-injection and the signal remained above detection level in 10 h. The fluorescence for **4** reached its average maximum intensity of 3.5×10^9 at 15 min and the signal remained above detection level in 10 h. For **2**, fluorescence intensity reached lower average maximum of 1.5×10^9 approximately at 15 min and then the signal was decreased below detection level by around three h post-injection.

Two-sided student's t-test was performed between average values of **12** and **8, 12** and **4**, **12** and **2** in the 2-48 h window and results show statistically significance between each pair (Fig. 2.6). Within the 2-48 h time window, the average tumor uptake of the hypoxia-targeted rigid dye (**12**) is 2.7 times that of the non-targeted rigid dye (**8**), 1.9 times that of the piperazine-2-nitroimidazole-ICG (**4**), and 7.2 times that of the biscarboxylic acid ICG (**2**).

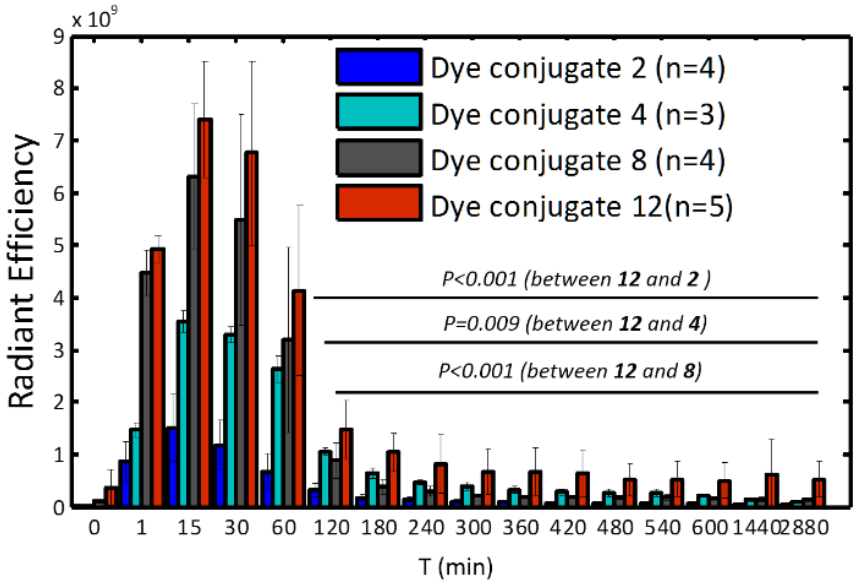

*Figure 2.6. Kinetics of tumor uptake and washout characteristics of **12**, **8**, **4** and **2**.*

2.3.4 Dye residue in tumor after 48 hours

All mice were sacrificed after 48 h post-injection. Tumor tissue were excised and imaged in the same imaging condition (Fig. 2.7). For mice injected with **2**, an average maximum fluorescence intensity of 0.4×10^8 was detected in the tumor. For mice injected with **4** and **8**, higher averaged maximum fluorescence intensity of 1.5×10^8 and 2.2×10^8, respectively, were detected in the tumor. The highest averaged maximum fluorescence intensity of tumor was in the group injected with the **12**, measured as 5.0×10^8.

Based on the *ex vivo* distribution study, the 48 h tumor uptake of the hypoxia-targeted rigid dye (**12**) is about 2.3 times that of the non-targeted rigid dye (**8**), 3.4 times that of the piperazine-2-nitroimidazole-ICG (**4**), and 14 times that of the biscarboxylic acid ICG (**2**). The two-sided student's t-test on the *ex vivo* tumor radiant efficiency data between hypoxia-targeted (**12**) and non-targeted rigid dye (**8**) is statistical significant (p=0.004).

By comparing the fluorescence radiant efficiency of the dye *in vivo* at 48 h post-injection (Fig. 2.6) and radiant efficiency of the *ex vivo* samples (Fig. 2.7), we observed similar or higher fluorescence intensity in the latter (*in vivo*: 5.3×10^8, 1.3×10^8, 9.7×10^7, 2.5×10^7 versus *ex vivo:* 5.0×10^8, 2.2×10^8, 1.5×10^8, 3.5×10^7, for each dye respectively). Since the *ex vivo* tumor imaging was performed on excised tumor without skin, it is reasonable to expect that the measured dye fluorescence intensity is similar or higher.

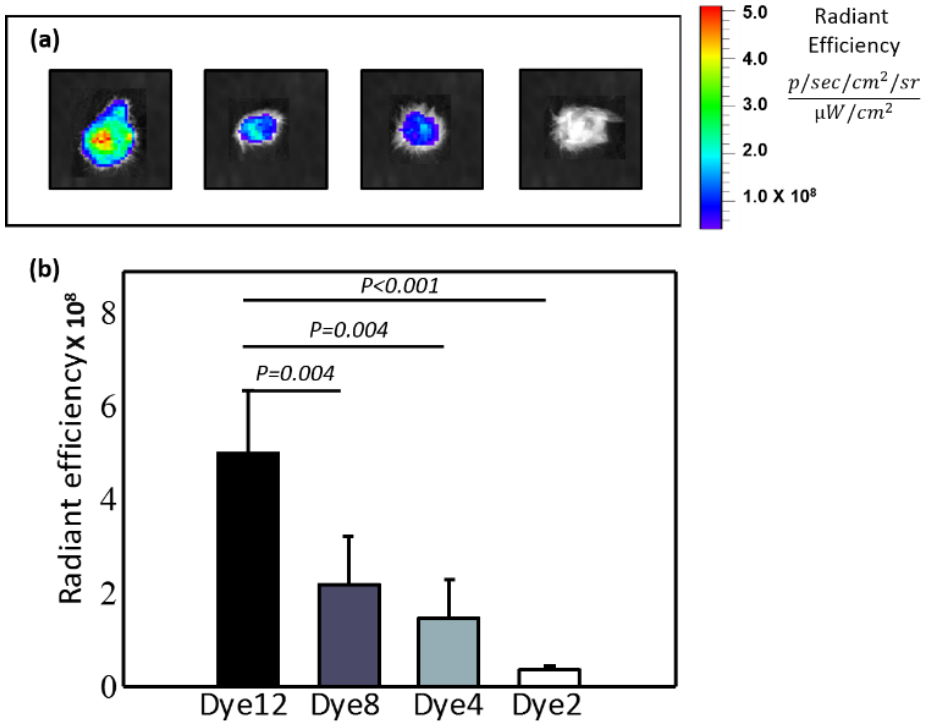

Figure 2.7. Ex vivo *experimental results. (a) Fluorescence images of excised organs from tumor bearing mouse injected with (from left to right):* ***12****,* ***8****,* ***4****, and* ***2****. (b) Statistical results in different groups of mice tumor.*

2.3.5 Immunohistochemistry (IHC) and dual labeling results

Typical fluorescence images labelled with pimonidazole hydrochloride-FITC (green, channel 2) and with hypoxia-targeted dye **12** and non-targeted rigid dye **8** (red, channel 1), are shown in Fig. 2.8 top and middle row respectively. The targeted rigid dye **12** labelled area is mainly located in the center region and correlates with the region labelled with pimonidazole hydrochloride-FITC; while the non-targeted dye **8** labelled regions are scattered and showed no significant overlap with the region labelled with pimonidazole hydrochloride. On average, the correlation coefficient between channel 1 and channel 2 images of **12** and **8** is statistically significant ($p<0.05$) as shown in Fig. 2.8 (g).

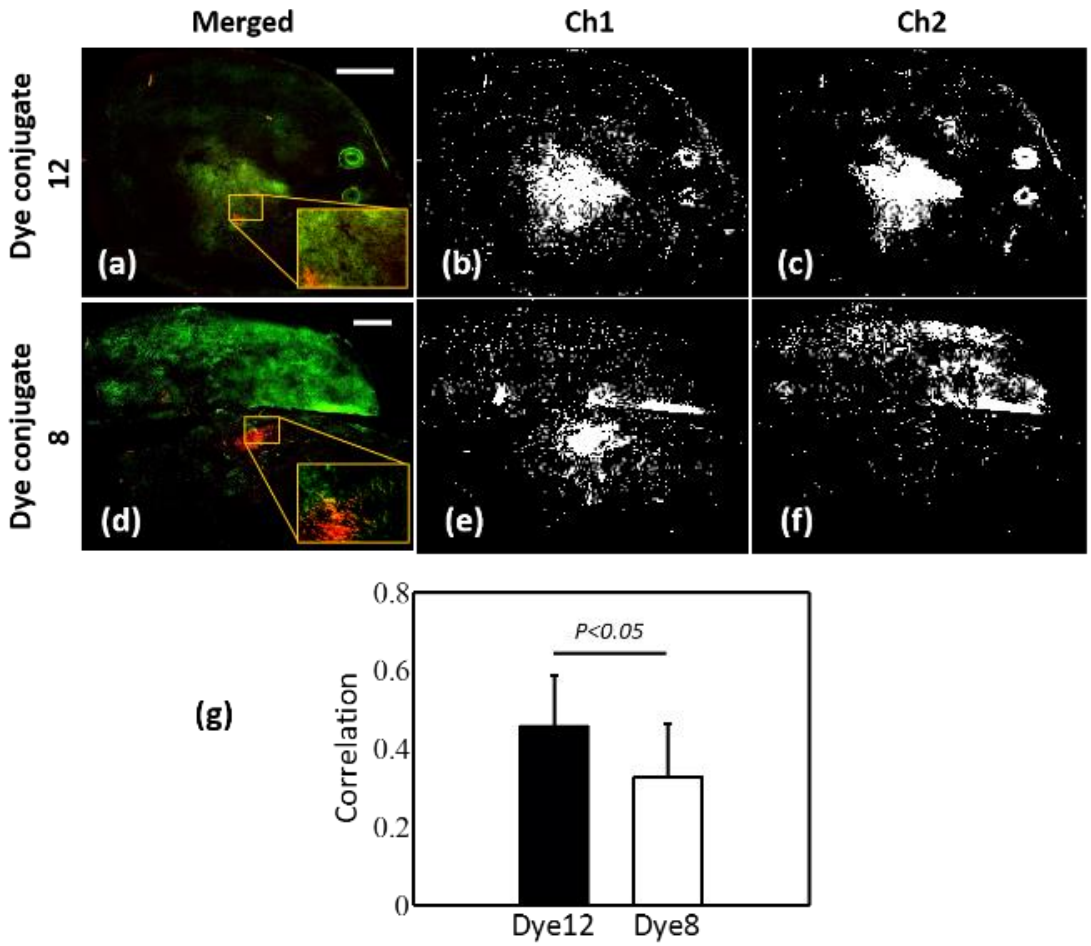

*Figure 2.8. IHC results. Top row: (a) Typical overlaid fluorescence image labelled by hypoxia-targeted rigid dye **12** (red) and commercial lpimonidazole hydrochloride (green). (b) Binary image acquired through microscope channel 1 (Cy5) after processing with 11-12% threshold. (c) Binary image acquired through microscope channel 2 (FITC) after processing. Middle row: (d) Typical overlaid fluorescence image labelled by non-targeted rigid dye **8** (red) and pimonidazole hydrochloride (green). (e) Binary image acquired through microscope channel 1 (Cy5) after processing. (f) Binary image acquired through microscope channel 2 (FITC) after processing. The scale bars in (a) and (d) indicate 1 mm. Bottom row: (g) Correlation coefficients computed between Ch1 and Ch2 binary images (hypoxia-targeted rigid dye n=12, non-targeted rigid dye n=8).*

2.3.6 4-nitroimidazole dye testing results

The absorption and fluorescence spectra for piperazine-4-nitroimidazole-ICG dye-conjugate (**6)** were also determined using a Varian Cary 50 UV-Vis spectrophotometer. It shows dye **6** having a maximum absorption peak of 755 nm and emission peak at 790 nm.

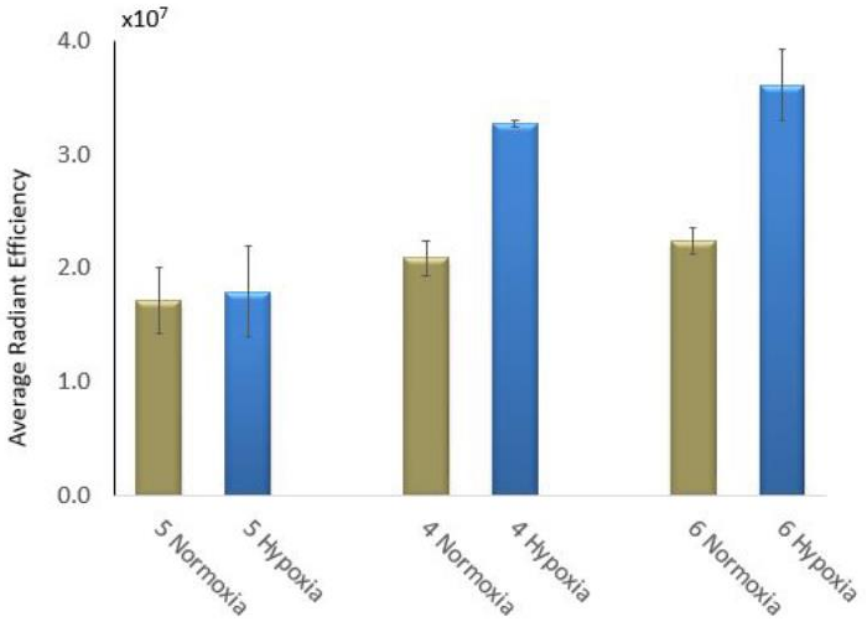

*Figure 2.9. Average fluorescent radiant efficiency of the hypoxic and normoxic dishes of 4T1 breast cancer cells treated with **5**, **4**, and **6** [28].*

Based on the *in vitro* cell experimental results, Fig. 2.9 shows the average radiant efficiency of the hypoxic dishes treated with imidazole-ICG **5,** piperazine-2-nitroimidazole-ICG **4**, and piperazine-4-nitroimidazole-ICG **6**. A slightly higher fluorescence yield (about 1.1-fold increase) was detected for the dishes injected with **6** compared with **4** under hypoxic conditions and a 2-fold increase when compared with **5**.

Fig. 2.10 shows the *in vivo* fluorescence distribution of a mouse injected with 100 µL at 25 µM concentration of dye **6**, **4**, and **5** over 48 hours. It shows a rapid uptake of the dye-conjugate in the tumor, as well as widespread distribution in the mouse. Washout is rapid in each case, but both **4** and **6** are retained in the tumor for a prolonged time relative to **5**. Based on the evaluation of quantitative dye change as a function of time, the fluorescent intensity for **6** is higher with an uptake of about 1.5-fold increase compared to **4**, and about 2.5-fold higher than **5** at the 15 min peak post-injection. Strong fluorescence intensity was still detected three h post-injection of **6**, which corresponded to about a 1.3-fold increase over **4**, and a 1.6-fold

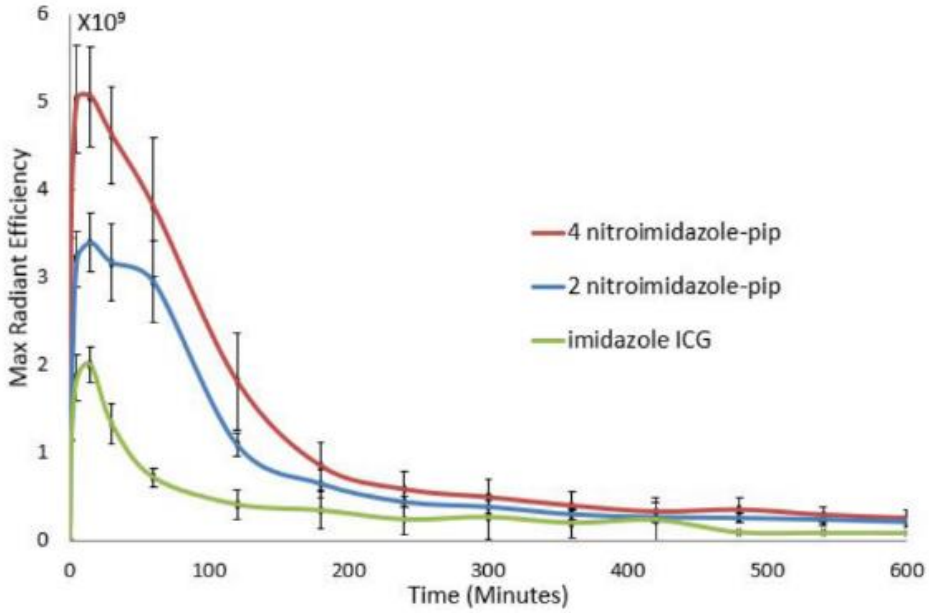

*Figure 2.10. Average maximum radiant efficiency change in tumor injected with piperazine-2-nitroimidazole-ICG **4**, imidazole-ICG **5**, and piperazine-4-nitroimidazole-ICG **6** [28].*

increase over **5**. At 48 h post injection, **6** was detected at a similar rate as **4**, and both were measured at about 11 times higher than the background. The difference of tumor fluorescence intensity averaged over 0-48 h period between the **6** and **4** show no significant difference ($p=0.29$) and significant difference between **6** and **5** ($p=0.03$).

Fig 2.11 shows the average hypoxic area percentage analyzed with stained tumor sections from mice treated with **4**, **6**, and **5**, by IHC method. Our results show no statistically significant difference of hypoxic area percentage between the **6** and **4** ($p=0.35$), and between **6** and **5** ($p=0.87$).

Fig. 2.12 shows the average integrated fluorescence density over the tumor sample area injected with dye **4**, **6**, and **5**. These results indicate similar fluorescence properties for both **6** and **4**. The difference of tumor-integrated density between **6** and **4** was not statistically significant ($p=0.62$). However, significant difference was observed between **6** and **5** ($p=0.0001$).

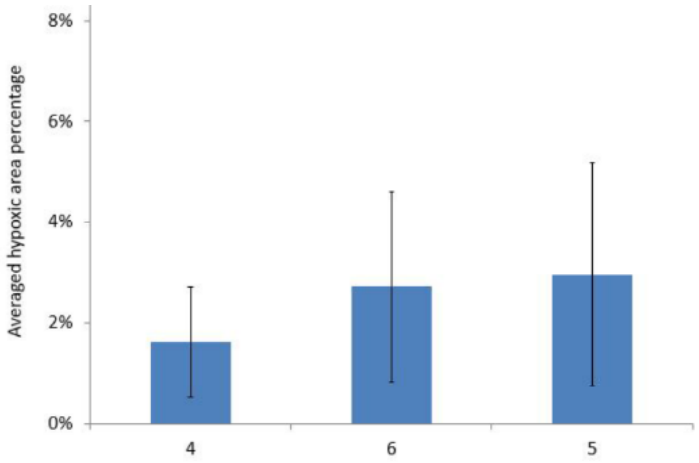

Figure 2.11. Averaged hypoxic area percentage calculated on all IHC stained tumor slices [28].

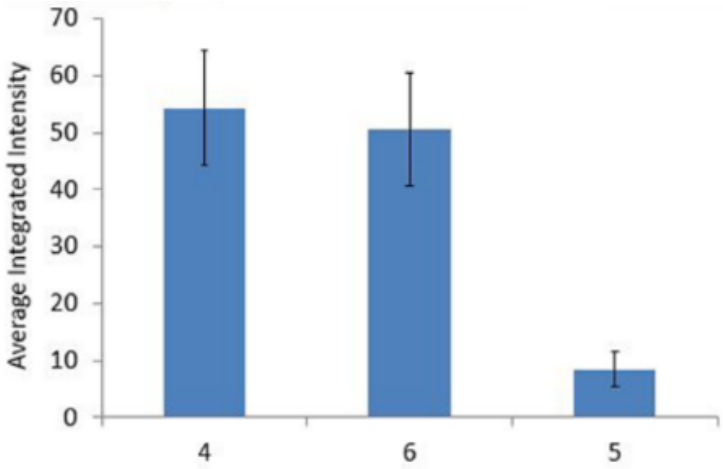

*Figure 2.12. Comparison of average integrated fluorescence intensity calculated with Li-COR images of mice tumor sections injected with **4**, **6**, and **5** [28].*

2.4 Discussion and conclusion

As anticipated, our results show that higher fluorescence intensity is achieved with rigid dye **12** as compared with the second generation dye **4**, although the absorption/emission wavelengths shifted ~100 nm from the second generation dye: from 755/780 nm to 657/670 nm (see Fig. 2.4). The fluorescence quantum yield of rigid dyes was measured to be about 0.4, which is around 5 times higher than that of the second-generation dyes. We believe that the

reason for the spectrum shift and quantum yield increase of the rigid dye **8** and the dye-conjugate **12** is due to the more rigid structure of the polyene chain, but the specific structural feature that correlates with these changes is unknown at this time [23].

Ex vivo florescence images of the sliced tumor tissue indicate that the dye molecules were not only distributed in tumor periphery area, but also penetrated throughout the entire tumor. Although the specific molecules this probe is binding to are yet to be investigated, from the report of other 2-nitroimidazole conjugated dye studies [37], we anticipate that this finding is due to the presence of nitroimidazole moiety. It is known that 2-nitroimidazole derivatives are trapped in the cells under hypoxic conditions, and our results are consistent with similar behavior for **4** and **12**.

Despite the high retention of piperazine-2-nitroimidazole-linked dyes **4** and **12** in the tumor region, results also show higher fluorescence intensity in the kidney and liver 48 h post-injection. In general, as reported by previous references that the 2-nitroimidazoles bind to rats liver in the hypoxia region [38], we believe this should be due to the hypoxia targeting of 2-nitroimidazoles. And moreover, as we observed concentrated fluorescence dye contained in the mice urine, and some reports indicated that ICG was selectively bound to the liver, later excreted in the bile due to its binding with serum proteins and then eliminated by giving bile to the feces [39, 40]. We therefore expect that this soluble dye conjugate is mainly washed out through the kidney and also removed through liver and gall bladder, and the binding of our dye to these two organs might be partially resulted from this reason. Although during the experiment, no observable difference was found for the mice injected with dye **2**, **4**, **5**, **6**, **8** or **12**, based on post-injection activity or weight loss, suggesting that there is no significant short-

term toxicity with the mice injected, more studies are needed to confirm and exploit our understanding on the binding mechanisms behind.

The correlation between the dual-channel labelled images was performed after applying a threshold to binary images. By varying the threshold from 8-20%, we found that a lower threshold can cause a large variation among tumor samples due to noise. The best threshold was found to be 11-12%.

Lastly, it was demonstrated in the results that the efficacy of 4-nitroimidazole-ICG (**6**) as a hypoxia targeting fluorescence probe. In vitro cell study and *in vivo* studies showed both **6** and **4** dye-conjugates retained to a great extent in hypoxic tumors when compared with imidazole derivative **5**. The Li-COR imaging and IHC results confirmed similar fluorescence properties between **6** and **4**. Further studies are required to illuminate the retention of **5** in the tumors. Future study may focus on toxicity of 6, though no short-term toxicity issue was observed.

In summary, we evaluated the new generation hypoxia-targeted rigid dye that has a higher fluorescence quantum yield. Results show more than twice in vivo tumor fluorescence intensity comparing with 2-nitroimidazole-ICG. We have also demonstrated comparable hypoxia targeting performance of **6** and **4** and better than the imidazole derivative **5**. Our initial data suggests **6** is applicable as a hypoxia probe with significant cost reduction in synthesis. Retention of **5** in tumors suggests possible other factors for its uptake by the tumor.

Chapter 3 Toward mechanism of our dye binding: the biotin dye study

3.1 Introduction

In the previous studies, we did extensive experiments to systematically investigate the performance of our three generations of indocyanine-dye conjugates on the fluorescence labeling of tumor cells. Almost all the results from *in vitro* cell studies, *in vivo* mice experiment and *ex vivo* tissue investigation suggested our dyes with the 2-nitroimidazole moiety remains in the tumor tissue significantly more than the dyes without the 2-nitro or 2-nitroimidazole moiety (Figs. 2.5, 2.6, 2.7, 2.8, 2.10 and 2.12). Further, from the *in vitro* cell studies, the binding of dyes with 2-nitroimidazole moiety to the tumor cells is observably higher in hypoxia condition than normoxic condition (Fig. 2.9). Moreover, the commercial Hypoxyprobe™-1 stained areas on the *ex vivo* tumor tissue slides and our 2-nitroimidazole-dye stained areas are generally overlapped with each other (Fig. 2.8 (a)-(c)). But there is little direct proof form our results that our 2-nitroimidazole-dyes bind to tumor hypoxia and we do not know to which molecule(s) these dyes bind to. Also, we need explanation on the dye residues in other organs such as kidney and liver. Is it also mainly due to the hypoxia? With these questions, we continued our study with a biotin-linked 2-nitroimidazole dye for obtaining deeper understanding on the mechanism.

A literature review shows that the 2-nitroimidazoles and its binding to the hypoxia tissues have been studied for long in the biochemistry field, and many information are given by their reported results. An early report in 1976 by Varghese *et al*. showed that the 2-nitroimidazoles bind to hypoxia cells *in vitro* and *in vivo* [41]. According to another *in vivo* experiment, the binding of 2-nitroimidazoles to the acid-insoluble fractions of EMT6 tumors in balb/c mice amounts to be 2% of the radioactively labeled misonidazole (one derivative of 2-

nitroimidazoles, as shown in Fig. 3.2 Ia) injected into mice [42]. By combining the previous study report that one-half of the 2-nitroimidazole moiety excreted unchanged [43], approximately 4% of the metabolized 2-nitroimidazoles was bound to tumor cell macromolecules [44]. In the 1980s, Raleigh *et al*. did an *in vivo* experiment with the CCI-103F (a radioactivity marked 2-nitroimidazole), and showed the NMR signal from CCI-103F in liver is 3-4 times that of tumor [45].

Many studies of the 2-nitroimidazoles focused on confirming the marking area in tissue is the hypoxia area in tumor and normal tissues. Van Os-Corby *et al.* [46] studied with radiatively marked misonidazole and reported that the binding rates and the oxygen concentration for half-maximum binding of misonidazole to liver tissue was not significantly different from that for brain, heart and tumor tissues. In further step, Cline *et al.* used IHC technique and showed the binding of 2-nitroimidazole marker to the hypoxia area occurring in the cytoplasm of canine tissues cells, and the binding occurs 10-12 cell diameters away from the tumor blood vessel (Fig. 3.1) [47].

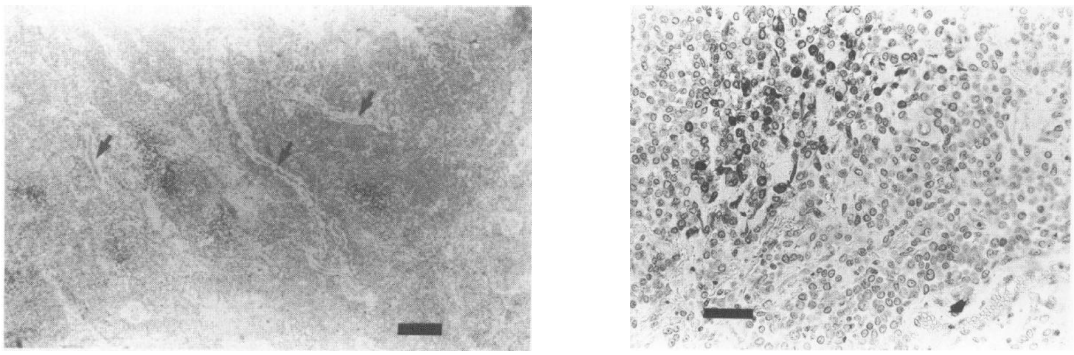

Figure 3.1. Immunoperoxidase labeled section of excised canine mast cell tumor after in vivo labeling with CCI-103F. Left, bar = 250 µM and right (the magnified image), bar = 50 µM. The black arrows indicate blood vessel location. [47]

For studying the mechanism, Miller *et al.* and Raleigh *et al.* did some *in vitro* experiments and indicated that the primary binding is to the proteins[44, 48] with both the side chain and

imidazole ring involved, although the consumption of 2-nitroimidazoles may follow various pathways [49]. Later, Raleigh *et al.* [44] found that the binding of reductive 2-nitroimidazoles was most efficient to the protein whose disulfides have been reduced to the thiol groups, or peptides with the thiol groups such as glutathione and cysteine. In their study, they used chemical procedures by adding the 2-nitroimidazoles (tritium of Misonidazoles, Fig. 3.2 Ia, and CCI-103F, Fig. 3.2 Ib) into solutions containing the bovine serum albumin (BSA) which has disulfides, phosphate buffer and sodium formate and put under hypoxia condition. They induced the 2-nitroimidazoles reductive activation and binding by radiation, then detected the thiol content (with Ellman's reagent detected at 410 nm) and 2-nitroimidazoles binding with BSA (by detecting the Misonidazoles at 320 nm and by scintillation counting of CCI-103F). Results showed protein thiol formation increased sharply just at the point where increased binding occurred, and the thiol groups binding to 2-nitroimidazoles are more than twenty times more effective than other proteins or nucleophilic groups. By comparing their results with previous reports, they formulated the mechanism by which the reductively-activated 2-nitroimidazoles bind to macromolecules in hypoxia cells, as shown in Fig. 3.2. The 2-nitroimidazoles are first reduced under hypoxia condition to the form of chemical II in Fig. 3.2, and then bind to the protein with thiol group (IIIa and IIIb), at 4 or 5 positions of the imidazole ring of reductively-activated 2-nitroimidazoles), or form reversible hydrolyted compound (IV) with peptides such as lysine and arginine. Their results showed around 20% of the consumed 2-nitroimidazoles are bound through path III, and path VI (accounts for 38% of the consumed 2-nitroimidazoles) is related to the toxicity of the reduced 2-nitroimidazoles. At the end, they mentioned that a complete understanding of the mechanism(s) of binding would require that the structure of the protein adducts be determined.

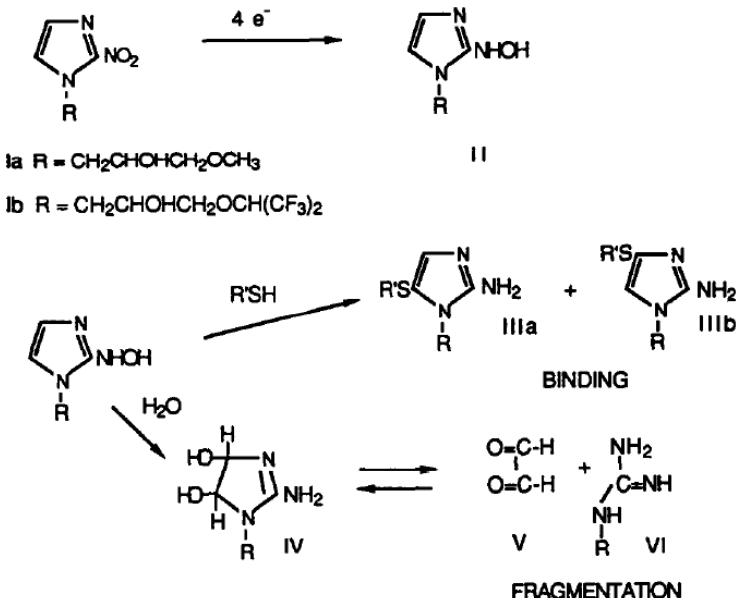

Figure 3.2. Major pathway of reductive 2-nitroimidazoles and binding to macromolecules [44].

In a later paper, Arteel *et. al* [38] studied the pimonidazole (one derivative of the 2-nitroimidazoles) binding to rats hypoxia liver by looking at the binding area with oxygen perfused anterograde or retrograde direction, and Gavon *et al.* [50] studied by regulating liver oxygen tension with KCN treatment (can inhibit mitochondrial respiration, thus leads to hypoxia). They both used IHC method for the detection of liver tissue pimonidazole-protein binding. They showed the pimonidazole binding to the hypoxia proteins is regulated directly by the O_2 concentration and gave a completed mechanism of this binding, as displayed in Fig. 3.3. With adequate oxygen, the pimonidazole can be oxidized by catalyst (cytochrome P-450) to pimanidazole N-oxide (Fig. 3.3A), or form conjugate by glucuronyl- or sulfo- transferase (GT or ST in Fig. 3.3B). It can also get electron from NADH (Nicotinamide adenine dinucleotide, a reducing agent) or NADPH (Nicotinamide adenine dinucleotide phosphate, a reducing agent) to form the radical intermediate (Fig. 3.3C) and be re-oxidized by the oxygen. However, in the hypoxia condition it is further reduced to the hydroxylamine intermediate (Fig.

3.3D) and binds to any macromolecules (proteins, peptides and amino acids) that contains the thiol group (-SH) (Fig. 3.3F). They concluded by that the binding of reductive pimanidazole is not dependent on the pyridine nucleotide redox state (NADH or NADPH concentration), but dependent on the micro-environment oxygen concentration, so the binding reflects low oxygen in liver cells and is valid technique for quantifying hypoxia in liver tissue.

Based on our review, the binding is towards the macromolecules (proteins, peptides and amino acids) with thiol groups in hypoxia cells in a non-reversible direction. As the thiol group is not limited to certain type of protein, the binding should not target only one protein or peptide.

The critical step for solving our questions mentioned at the beginning of this chapter is to identify the proteins that are bound by our 2-nitroimidazole dyes. From the previous study, we had one time result from protein analysis with tumor extract showing one fluorescent band by gel electrophoresis, which means one group of proteins were found with our 2-nitroimidazole-ICG dye-conjugate bound. In order to further identify the protein type, Dr. Smith's lab has synthesized the biotin dye with one of the two arms of the 2-nitroimidazole substituted by the biotin moiety. Theoretically, by using the specific reaction of avidin-biotin, the protein binding to the biotin dye can be separated for later identifying. A half-loaded dye with only one arm linked with the piperazine-2-nitroimidazole moiety was also synthesized for comparison.

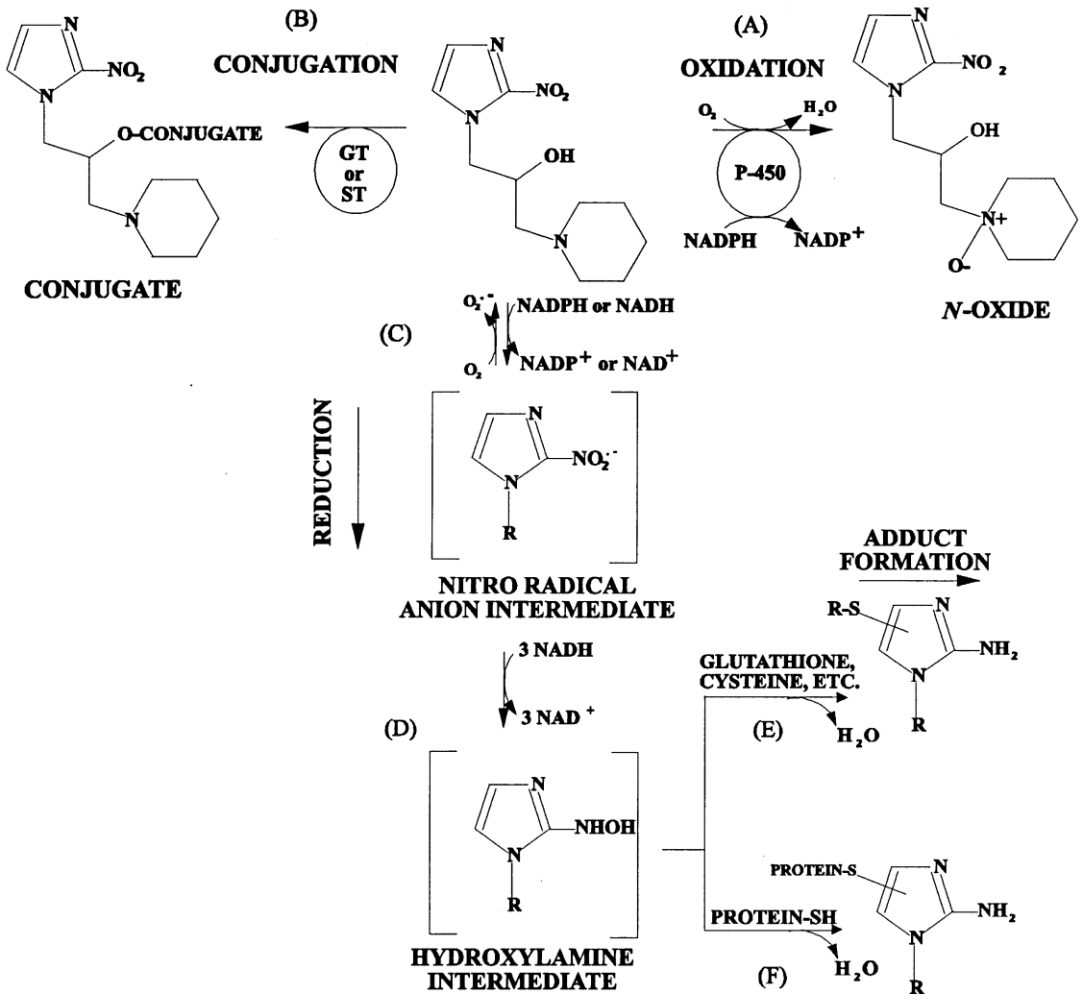

Figure 3.3. Schematic representation of metabolism of pimonidazole in tissue [50].

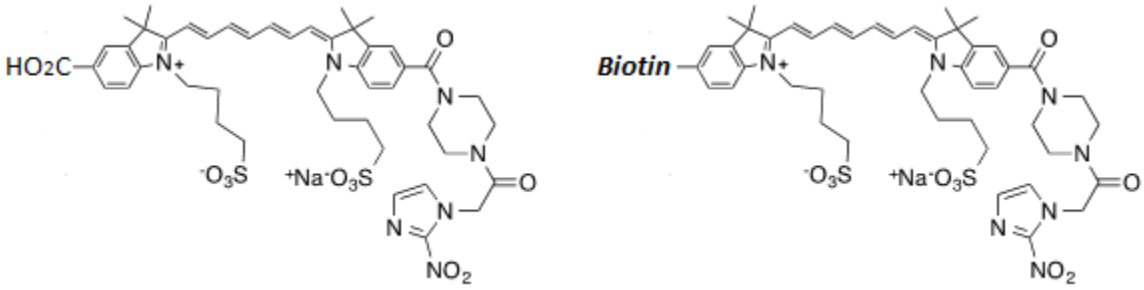

Figure 3.4. Molecular structure of the half-loaded dye and biotin dye

3.2 Methods

We studied the *in vivo* fluorescence signal in tumor by injecting the biotin dye into the mice and compared with dicarboxylic acid ICG (Fig. 2.1, dye **2**), piperazine-2-nitroimidazole ICG (Fig. 2.1, dye **4**) and the half-loaded dye (Fig. 3.3 left). Following similar procedures as in Chapter 2, mice were monitored after the injection of 100 µl dye **2** (n=4), half-loaded dye (n=2), dye **4** (n=3) and the biotin dye (n=2) at 25 µM concentration. The tumor was excised from mice immediately after sacrificing the mice 48 h after dye injection. And the tissue samples were fresh frozen with liquid nitrogen and saved at -80°C.

Later experiments (cell lysis and protein analysis) are mainly carried out by our collaborator Dr. Yao's group in UConn department of Chemistry. Currently two ongoing experiments are performed. In the first one, tumor tissues are blended to get extract with water-soluble proteins. The mixture (cell fragments with buffering solution) were then centrifuged and the supernatant were taken out for the SDS-PAGE analysis. The SDS-PAGE (sodium dodecyl sulfate polyacrylamide gel electrophoresis, a western blot method) method is used to examine the existence of 2-nitroimidazole bound proteins by electrophoresis using the polyacrylamide gel as a support medium. In the second one, part of the supernatant was passed through the advin-enriched column, through which the dye-protein complex is separated and purified. Then the bound complex is washed down and analyzed again with the SDS-PAGE method, and to be imaged to identify the targeted protein molecules.

After processing, the SDS-PAGE gel with protein loaded was imaged using the Odyssey Infrared imaging system (Li-Cor imager), as described in part 2.2.3. This work was done by another member from our lab. Comparison was made among mice tumors injected with piperazine-2-nitroimidazole ICG, biotin dye and the control (without injecting any dye). Note

that as the first round test with mice injected at 25 μM dye concentration did not show promising result due to the weak signal that can be barely acquired by the Li-Cor imager, for later analysis we increased injection concentration to 50 μM.

3.3 Results and Discussion

The optical absorption and emission peaks as well as the extinction coefficient of the biotin dye and half-loaded ICG were measured and listed with previous measurements in Table 3.1 [26]. The absorption and fluorescence emission peaks appear to be similar to those of the ICG dyes and are about 100 nm longer than the rigid dye, while the extinction coefficient is close to half of the bis-carboxylic acid ICG and pip-2nitroimidazole ICG and close to two-third of that of the half-loaded ICG, which might be related to the increased molecule size.

Table 3.1 Optical properties of the biotin dye in comparison with the previous dyes

Compound	**λ_{abs} (nm)**	**λ_{em} (nm)**	**Extinction coefficient ($M^{-1}cm^{-1}$)**
Bis-carboxylic acid ICG	755	790	221,000
Half-loaded ICG	755	790	170,994
Biotin dye	755	785	102,000
Pip-2nitroimidazle ICG	753	790	230,000

A quantitative comparison of *in vivo* tumor fluorescence intensity is shown in Fig. 3.5. From the result, the in vivo tumor fluorescence intensity reaches its peak at 5-15 min post-injection, and is quickly washed out after the peak. The average tumor signal in 1-60 min time range for biotin dye injection is the lowest compared with other ICG dyes, which might be explained by the combined effect of the dye's optical property and diffusing to the tumor tissue. After 60 min, the signal from biotin dye is similar with that of the half-loaded dye, less than

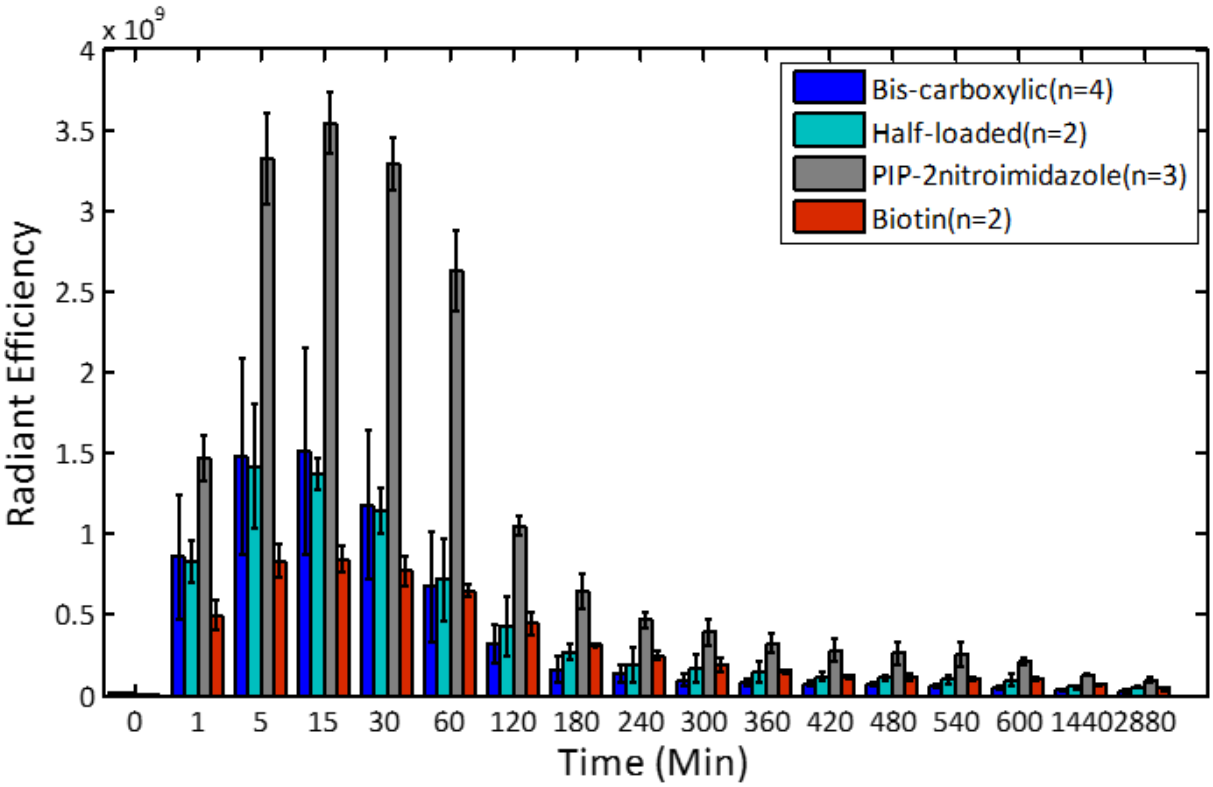

Figure 3.5. Tumor fluorescence intensity change over time with four dyes injected.

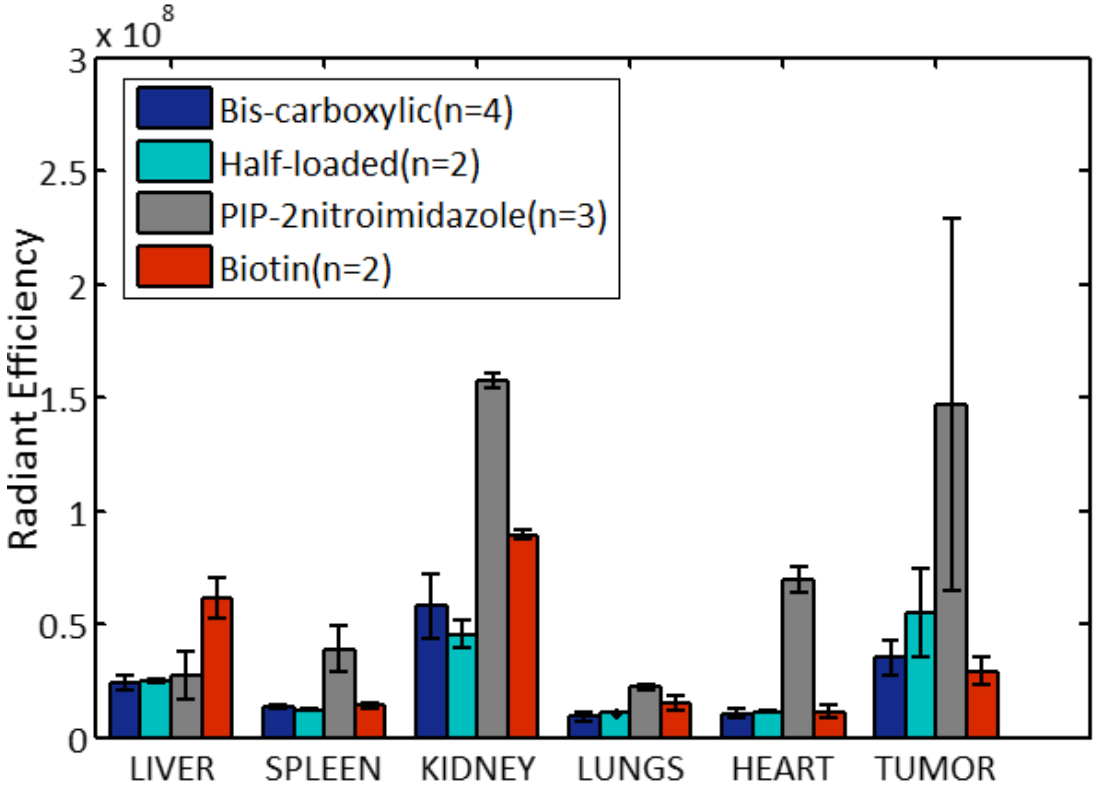

Figure 3.6. Ex vivo tumor and organs fluorescence intensity with four dyes injected.

the piperazine-2nitroimidazole ICG, but higher than the bis-carboxylic acid ICG, which might be explained by the effect of hypoxia targeting by the single arm of 2-nitroimidazole link.

The *ex vivo* fluorescence images from different organs after being excised form the sacrificed mice were also acquired, and a quantitative signal intensity plot of the averaged data from different groups were shown in Fig. 3.6. The excised tumor signal is a little different from the in vivo tumor signal at 48 H (as shown in Fig. 3.5), in that the fluorescent signal for biotin dye is the lowest and similar to the bis-carboxylic one. The strongest signal still comes from the kidney, and then from the liver and tumor.

The Li-Cor imaging results with 50 μM dyes injected are shown in Fig. 3.7. Current results show fluorescence coming from one band (as indicated by arrow) in the SDS-PAGE gel loaded with mice tumor proteins for mice injected with the biotin dye and piperazine-2-nitroimidazole ICG, but not in the control columns. Fluorescence intensity from piperazine-2-nitroimidazole injected mice is shown similar to that from the biotin dye injected ones. These bands existed only in the gel for tumors with dye injected indicate the existence of proteins that bind to the biotin or piperazine-2-nitroimidazole dye.

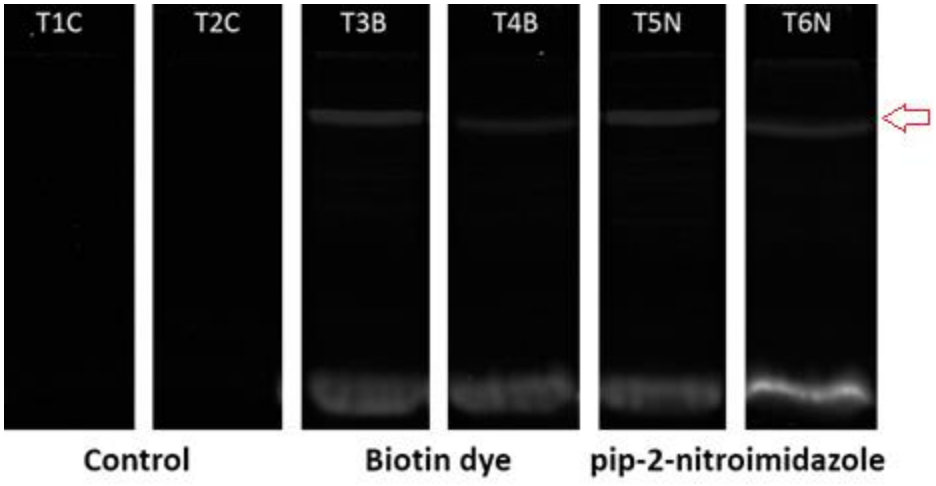

Figure 3.7. Tumor extract fluorescence image

3.4 Conclusion

The optical properties of the biotin dye and half-loaded dye were measured. The *in vivo* and *ex vivo* test with dye injected mice tumors shows lower signal coming from the biotin dye compared with the piperazine-2-nitroimidazole ICG, which may be explained as the effect of one arm linked with the 2-nitroimidazole moiety. The fluorescent bands in SDS-PAGE gel loaded with proteins extracted from tumor injected with the biotin and piperazine-2-nitroimidazole dyes suggest a promising way of identifications of exact proteins bound by our dyes. Further steps are need to be taking to identify exact bound proteins.

Chapter 4 Improving breast cancer diagnosis by reducing chest wall effect in ultrasound guide diffuse optical tomography

4.1 Introduction

4.1.1 DOT systems

The diffuse optical spectroscopy or tomography (DOS or DOT) are used to measure the optical properties of biological tissue by using diffuse light, whose light rays propagate at different angles after interacting with tissues. This technique is based on the diffusive theory to relate changes in tissue optical properties to the diffuse light change. High sensitivity, safety and low cost are among the most significant advantages compared with the conventional techniques. They are also able to provide functional image or information of investigated tissues [51]. In current clinical study, human joint, brain, breast and prostate are among the most studied subjects for DOS/DOT, as they don't require too deep penetration of light in these structures.

In a DOS system, a measurement can be simply taken with a light source and a detector placed on the surface of investigated tissue. According to diffusive theory, properties of a homogeneous medium can be decided by measurements taken at two relative source-detector locations. In a DOT system, where the optical property images are generated, a couple of sources and detectors are used at different geometries. The spatial resolution is limited (suggested 5:1 for tissue thickness relative to detectable anomaly size in diffuse imaging) due to the ill-posed problem [51]. Increasing the number of source and detector pairs can remedy this problem, but the cost and acquisition time also need to be considered in deciding the source and detectors used. Another consideration is the layout of sources and detectors. This is usually decided by the object's shape and dimension. Acquisition geometries used by breast diffuse optical imaging include the transmission (planar or ring shaped) or reflection mode. Based on

the signal used for measurement, current diffuse optical systems can be categorized into three major categories: systems based on the frequency-domain (FD) signal [52], direct current (DC) signal [53] or time-resolved (TR) signal [51, 54]. In the following part, detailed introduction is given on the data processing principles of FD system, which method is used in our DOT system. And brief introductions are given on the DC and TR systems.

FD system

The frequency domain system measured the re-emitted light in a broad bandwidth with the light source set at different frequencies. Source light intensity is modulated by AC signal at radiofrequency (3kHz to 300GHz) [55], and the amplitude and phase changes are measured in the detected signal.

Based on the theory of diffused photon density wave [52], given a pencil beam incident light and semi-infinite turbid medium, the spatial energy density of diffusive wave at position $\bar{r}$ is

$$U(\bar{r}) = \frac{S}{4\pi D}\left[\frac{e^{-ik|\bar{r}-\bar{r_s}|}}{|\bar{r}-\bar{r_s}|} - \frac{e^{-ik|\bar{r}-\bar{r_i}|}}{|\bar{r}-\bar{r_i}|}\right] \tag{4.1}$$

Where S is the source intensity. The wave number $k^2 = \frac{-\nu\mu_a + i\omega}{D}$ and the light diffusion coefficient $D = \frac{\nu}{3\mu_s'}$. ν is the light speed in medium and ω is the angular frequency of light. $\bar{r_s}$ and $\bar{r_i}$ are the real and imaginary point sources that are used as substitution for incident light. When the source-detector separation (ρ) is larger than the transport mean free path z_{tr}, eq. 4.1 can be simplified as

$$U(\rho) = \frac{S}{4\pi D}\frac{e^{ik\rho}}{\rho^2}\left[-2ik(z_b^2 + z_b z_{tr})\right] \tag{4.2}$$

Where the extrapolated boundary position $z_b = \frac{2}{3\mu_s'}$, and the mean free path $z_b = \frac{1}{\mu_s'}$.

From eq. 4.2 we can derive the linear amplitude and phase equations, and k_r and k_i can be fitted as the slopes of amplitude (logarithmic scale) and phase versus source and detector distance (Fig. 4.1).

$$\ln(\rho^2|U(\rho)|) = -k_i\rho + \ln(\frac{|S|}{2\pi D}[z_b^2 + z_b z_{tr}]\sqrt{k_i^2 + k_r^2}) \tag{4.3}$$

$$\Phi(\rho) = k_r\rho - tan^{-1}(k_r/k_i) + \Phi_{source} \tag{4.4}$$

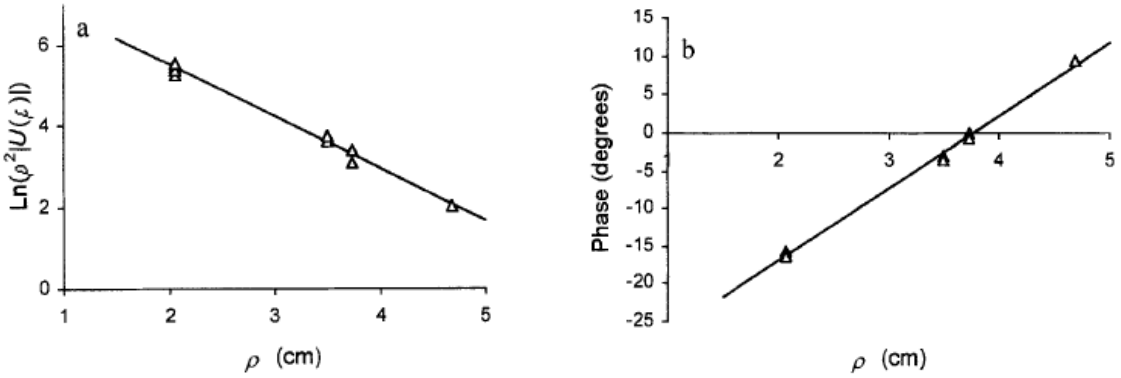

Figure 4.1. Typical fitting of k_i (left) and k_r (right) based on the amplitude and phase measurements [52]

The average absorption coefficient μ_a and the reduced scattering coefficient μ_s' can thus be derived

$$\mu_a = \frac{\omega}{\nu}[\tan(2tan^{-1}\frac{k_r}{k_i})]^{-1} \tag{4.5}$$

$$\mu_s' = \frac{k_i^2+k_r^2}{3\sqrt{\mu_a+(\omega/\nu)^2}} \tag{4.6}$$

Where ω is the modulation frequency and ν is the speed of light. Once the average measured μ_a and μ_s' are determined, reconstruction is made by dividing the medium into a number of 3D voxels. Each voxel optical property $\mu_a(r_v)$ and $\mu_s'(r_v)$ of the can be decided by [52]

$$\mu_a(r_v) = \frac{\sum_{sd} W(r_{sv},r_{vd})\mu_a}{\sum_{sd} W(r_{sv},r_{vd})} \tag{4.7}$$

$$\mu_s'(r_v) = \frac{\sum_{sd} W(r_{sv}, r_{vd})\mu_s'}{\sum_{sd} W(r_{sv}, r_{vd})} \tag{4.8}$$

Where the weight matrix is computed through Green Function: $W(r_{sv}, r_{vd}) = -U_0(r_{sv})G(r_{vd})/D$.

DC system

For these systems, only DC measurements are needed to reconstruct tissue optical images. The image reconstruction includes the process of solving both the forward and inverse problems.

In the forward problem, the diffuse equation of light in highly scattering medium is

$$\nabla \cdot D(r)\nabla\Phi(r,\omega) - \left[\mu_a(r) - \frac{i\omega}{c}\right]\Phi(r,\omega) = -S(r,\omega) \tag{4.9}$$

Where $\Phi(r,\omega)$ is the photon density at position r, ω is the light modulation frequency and $S(r,\omega)$ is the source term. In DC system ω is usually zero, but sometimes it is modulated at low frequency (e.g. kHz) to improve the SNR or to encode different sources [55]. As shown in Fig. 4.1, in solving the forward problem, Chen *et al.* used finite element

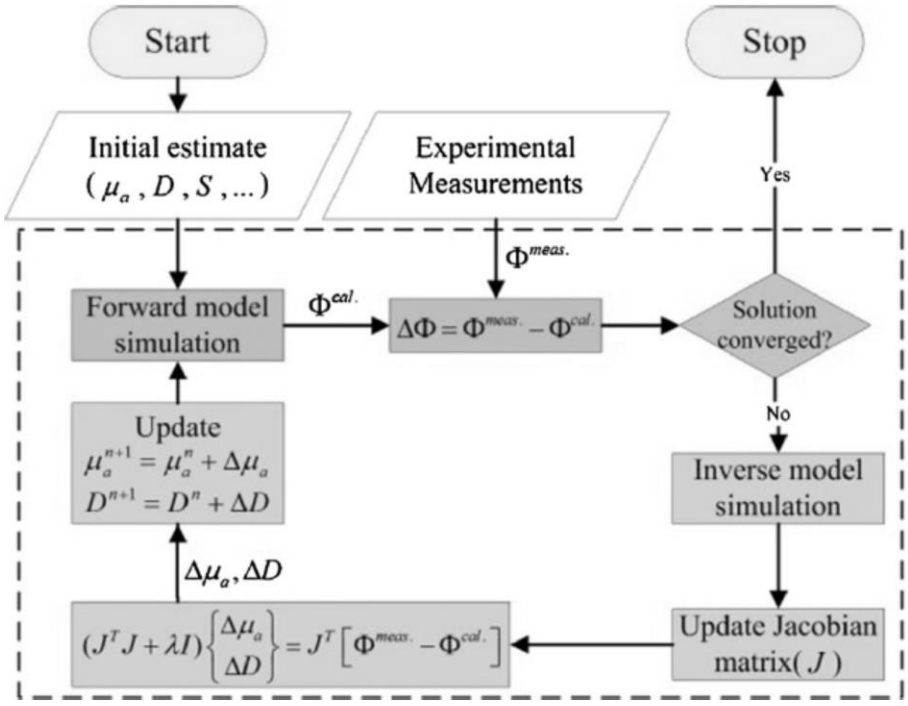

Figure 4.2. Flow chart of DC system image reconstruction [53].

method to get Φ^{cal} with the initial estimate of μ_a and D [53]. Then the difference ($\Delta\Phi$) between measurement Φ^{meas} and forward solution Φ^{cal} is computed minimized by iterative updating of μ_a and D. The searching step is an inverse problem and the solution is based on the regularization method. Here the Tikhonov regularization method was used, in which $\Delta\mu_a$ and ΔD can be related to $\Delta\Phi$ by the Jacobian matrix (*J*) and regulating factor λ.

TR system

In the time-domain mode, temporal responses to an ultrashort laser pulse are measured around the measured subject to be imaged. The source light is an ultra-short pulse (in *ps* range), and the detected light pulses are broadened in terms of time. The re-emitted signal equals to the convolution of three functions: point spread function (PSF) due to light propagation in scattering medium, pulse profile of laser beam, and impulse response of the detection system [55]. The PSF due to light propagation in scattering medium can be solved with detected signals and the known source and system response, so the optical properties of the medium can be obtained by analytical fitting of this PSF or through iterative forward simulation.

4.1.2 DOT for the breast tissue characterization

Diffuse optical techniques for its utility in breast cancer diagnosis and treatment monitoring have been investigated extensively in the past two decades [56-63]. One critical parameter in breast tissue characterization is the normal tissue optical properties. The CW, FD and TR method have all been used to measure bulk optical properties of normal breast. Experimental set-ups are mainly in three positions: 1) a supine or sitting position with a hand-held probe placed on top of the examined breast, referred as FD reflectance or TR reflectance measurement [64-67]; 2) a prone position with source and detector fibers distributed around the examined breast, refereed as mixed CW, FD or TR reflectance and transmittance

measurement or ring geometry [51, 58, 68]; and 3) a prone or a standing position with the examined breast sandwiched between source and detector plates, referred as FD transmittance or TR reflectance or transmittance measurement [69-75]. Here we summarized the reported breast tissue bulk μ_a and μ_s' in Table 4.1.

Using CW method with a ring geometry, Jiang *et al.* measured the breast tissue background optical properties (μ_a and μ_s') of three healthy volunteers and the normal breast tissue adjacent to a lesion of six patients.[51] The patients' race was not found to affect measured optical properties. And μ_a and μ_s' measured from breast tissue adjacent to the lesion were 0.072-0.110 cm^{-1} and 7.5-10.7 cm^{-1}, which were comparable to those from the healthy volunteers of μ_a = 0.035-0.085 cm^{-1} and μ_s' = 9.0-10.5 cm^{-1}. Using a FD reflectance with patients in a supine position, Shah *et al*. measured breast tissue optical properties of 14 healthy subjects [64]. Significant difference was found between the pre- and postmenopausal subjects (premenopausal: μ_a = 0.048-0.150 cm^{-1} and μ_s' = 8.3-11.0 cm^{-1} and postmenopausal: μ_a = 0.016-0.064 cm^{-1} and μ_s' = 6.7-8.6 cm^{-1}). Using similar technique, Cerussi *et al.* measured breast optical properties of 28 healthy subjects [65]. They found the hemoglobin, water and scatter power were on a decreasing trend with age for subjects older than 50. They also found the scatter power correlated with water concentration, and correlated negatively with lipid. Using a FD transmittance geometry, Durduran *et al.* measured the optical properties of 52 healthy volunteers [70]. Investigation was focused on the correlation of optical properties, blood volume and oxygen saturation (SO_2) with the body mass index (BMI) and age, and only a weak correlation was found between blood volume and BMI, and μ_s' and BMI. By using a FD system with a ring geometry, Poplack and Pogue *et al.* first measured 11 patients and later 23 healthy volunteers' breasts at five wavelengths within 660-808 nm [58, 76]. The total

hemoglobin (tHb) and μ_a were found to be significantly associated with the BMI and breast density, but no significant association between SO_2 and either BMI or breast density. Recently, Fang *et al.* measured the optical properties of 68 breasts from 49 healthy volunteers and later 138 normal breasts from 125 subjects using a hybrid CW/FD DOT system with a transmittance geometry. Their study was focused on comparing the DOT measurements of hemoglobin and scattering maps with co-registered X-ray images of different categories of breast tissues [74, 75].

By utilizing the TR reflectance method with a single wavelength and a single source and detector pair, Suzuki *et al.* studied 30 Japanese healthy volunteers and found a high correlation of the breast tissue μ_a and μ_s' with age, BMI and menstrual status [69]. Later, Svensson *et al*. used a portable TR system to study water, lipid and hemoglobin concentration variation of 36 normal subjects [66]. Their results also showed that larger source and detector separation (2 cm vs. 1.5 cm) resulted in higher tHb and SO_2 values measured. Using a similar method, Mo *et al*. measured breast optical properties of 19 healthy Singapore women, and reported high correlations of tissue μ_a, μ_s' and tHb with age, menopausal status and BMI [67]. Grosenick *et al*. developed a TR transmittance system using a single-fiber delivering and a single fiber-bundle collecting setup to measure breast tissue optical properties of 35 patients and later 87 patients with lesions [71, 72]. The tHb concentration and SO_2 were also studied by comparing tumor and background tissues. Using a similar method, Spinelli *et al*. reported the tHb, SO_2, lipid and water concentration from absorption spectrum of 113 measurements from both breasts of 150 subjects [73, 77]. Correlations of these physiological properties with age, breast thickness and BMI were found.

Table 4.1. Comparison of reported optical parameters for normal breast at NIR

Ref.	Method *[1]	Position *[2]	Probe *[3]	N*[4]	Location*[5]			λ (nm)	μ_a (cm^{-1})		μ_s' (cm^{-1})	
					H	NC	NS		Mean±Std	Range	Mean±Std	Range
Shah[64]	FD	Supine	Hand-held	14	14			647-956	--	0.016-0.150	--	6.7-11.0
Cerussi[65]	FD	Supine	Hand-held	28	28			672	--	0.025-0.125	--	6.8-10.5
				28	28			800	--	0.025-0.100	--	6.0-9.1
				28	28			806	--	0.025-0.100	--	5.8-8.7
				28	28			852	--	0.040-0.120	--	5.7-8.2
				28	28			896	--	0.075-0.160	--	5.5-8.0
				28	28			913	--	0.075-0.180	--	5.6-7.9
				28	28			978	--	0.075-0.310	--	5.4-7.8
Svensson[66]	TR	Sitting	Hand-held	36	36			786	0.041±0.021	--	8.0 ± 2.0	--
Mo[67]	TR	Sitting	Hand-held	19	19			785	0.050±0.015	--	10.53±1.20	--
				19	19			808	0.052±0.015	--	10.49±1.19	--
Jiang[51]	CW	Prone	Ring	9	3		6	785	--	0.035-0.110	--	7.5-10.7
Poplack[58]	FD	Prone	Ring	23	23			785	0.052±0.019	0.030-0.102	11.7±2.0	7.9-15.5
Suzuki[69]	TR	--	Plates -R	30	30			753	0.046±0.014	0.024-0.078	8.9±1.3	6.3-10.8
Durduran[70]	FD	Prone	Plates	52	52			750	0.046±0.024	--	8.7±2.2	--
			-T	52	52			786	0.041±0.025	--	8.5±2.1	--
				52	52			830	0.046±0.027	--	8.3±2.0	5.0-13.5
Grosenick[71]	TR	--	Plates	28			28	670	0.041±0.013	0.025-0.080	11.7±2.3	7.0-18.0
			-T	35			35	785	0.039±0.009	0.025-0.060	10.2±1.6	6.0-14.0
Grosenick[72]	TR	--	Plates	87			87	670	0.036±0.008	--	10.5±1.3	--
			-T	87			87	785	0.039±0.011	--	9.5±1.4	--
				8			8	843	0.036±0.005	--	8.4±0.4	--
				22			22	884	0.059±0.016	--	8.0±1.0	--
Spinelli[73]	TR	--	Plates	113			113	637	0.055±0.007	--	13.4±2.6	--
			-T	113			113	656	0.041±0.005	--	13.5±2.1	--
				113			113	683	0.042±0.013	--	12.9±2.3	--
				113			113	785	0.037±0.013	--	11.3±2.1	--
				113			113	912	0.110±0.021	--	11.4±2.6	--
				113			113	980	0.099±0.028	--	11.7±2.6	--
Fang[74]	CW/FD	Standing	Plates -T	49	49			830	--	--	7.5±0.8	--
Fang[75]	CW/FD	Standing	Plates -T	125		125		830	--	--	7.1±1.6	--

*[1] Method: Measurement techniques that were used: CW: Continuous wave, FD: Frequency domain, TR: Time-resolved.

*[2] Position: Patient position in measurement

*[3] Probe: Probe geometry for light delivery and collection. Plates: Breast is sandwiched between two plates, with source and detectors on the plates, T: transmission, R: reflectance.

*[4] N: Total number of subjects (healthy volunteers or patients) involved in the study.

*[5] Location: Location of the breast tissue that is measured: H: Healthy subjects, NC: Normal breast tissue of contralateral reference side of the patient, NS: Surrounding breast tissue of a lesion of the same breast.

4.1.3 Challenges and solution

We have developed Ultrasound (US)-guided FD-DOT technique using a hybrid hand-held probe for breast cancer diagnosis and treatment assessment, with the wavelengths in the range used by other groups summarized in Table 4.1 [62, 63, 78]. From measured light reflectance, lesion optical absorption maps at four optical wavelengths were reconstructed and the hemoglobin concentration maps of tHb, oxygenated hemoglobin (HbO_2), and deoxygenated-hemoglobin (Hb) were calculated [79]. Results have shown higher sensitivity and specificity in diagnosing early stage (Tis-T1) breast cancers from benign lesions [79]. Compared with the systems developed by other groups, our system using a hand-held probe with patients imaged in a supine position can be easily incorporated into a conventional US pulse-echo scanning with no need to adjust the probe size to fit patients' breast. However, to probe breast lesions in the depth range of 1 to 4 cm, the source-to-detector separation of 3 to 8 cm is needed. At this range of source-to-detector separations, the chest wall affects measurements of background tissue optical properties [80, 81].

We have developed several methods to minimize the chest wall effect, including a two-layer modeling [82] and a two-layer reconstruction method [83], and a two-step fitting and reconstruction with a dual probe measurements (a small probe for the first layer and a larger probe for both layers) [84]. Despite the promising results, the clinical application of these methods is limited due to their intense computation and a slower convergence rate [82, 84].

In a recent paper, Nobuko *et al.* reported the effect of chest wall on light reflectance measurements using their TR-DOS system with 3 cm source-to-detector distance, and showed a function characterizing the tHb concentration in terms of chest wall depth [85]. Based on their measurements, they reported the tHb concentration ranging between 10-90 μM, and this

range reduced to 10-30 μM by taking out cases whose chest wall depths were smaller than 2 cm.

In this study, we have evaluated the correlation between the fitted background tissue optical properties and the chest wall depth from a total of 297 patients measured with our FD-DOT system [86]. The background optical properties were measured from the contralateral reference breast at the mirror position of the lesion. This is a large patient population and has diverse lesion types. Therefore, results should be a valuable reference for research community in DOS and DOT breast imaging field. An automated chest wall depth detection algorithm was developed by one of our lab mates, to compute the chest wall depth for each patient from co-registered US images. The automatically detected chest wall depth was validated by an expert with US images. Using lesion tHb values reported in Ref. [79], we have subtracted the background hemoglobin level from each patient's tHb to improve diagnosis between malignant and benign lesions.

4.2 Materials and Methods

4.2.1 Study Subjects

A total of 297 female patients were evaluated in this study. All patients signed the informed consent and the study protocol was approved by local Institution Review Boards. All data reported in this study were de-identified according to the institution approved protocols. The clinical characteristics of study subjects can be found from Ref. [79]. Briefly, from the total 300 female patients included for analysis in the referenced study, three patients were further excluded because digital co-registered US images were not available. Of the 297 patients analyzed in this study, 12 individuals without US identifiable lesions at the time of DOT study were considered as control group. Of the rest, 6 patients have two lesions. Thus we have total

291 lesions from 285 patients for analysis (the mean age is 50 years, ranging from 17 to 94 years). Of the investigated lesions, 232 were diagnosed to be benign and 59 were malignant. The patients with benign lesions were further sub-categorized into 7 groups including: proliferative lesions (Prolif.), fibroadenoma (FA), fat necrosis and inflammatory changes (FN), fibrocystic changes (FC), cystic changes (Cyst), lymph node (LN), breast tissue and other benign categories. Among the 297 patients, 18 had US images revealing deep chest walls beyond 5 cm and cannot be estimated accurately. These patients were not used for analysis of chest wall effect on background tissue optical property measurements. 225 had disclosed their race (black n = 45, Asian n = 4, Hispanic n= 42 and white n = 134), of which 3 white patients have two measurements each at two different normal reference locations because their two breast lesions were at different quadrants. Thus, we have total 303 measurements from 297 subjects analyzed for lesion diagnosis, 285 measurements from 280 subjects analyzed for chest wall effect, and 228 measurements from 225 subjects analyzed for skin color effect on reflectance measurements.

4.2.2 US-guided DOT imaging and data processing

The specifications of our US-guided FD-DOT system used for this group of patient data acquisition can be found in Ref. [79, 87]. Briefly, the co-registered US images and optical measurements were acquired simultaneously first from a lesion breast and then from the contralateral normal breast at the mirror position as the lesion (Fig. 4.3 (a)). For each patient, the measurement location at lesion side was chosen that the lesion was located in the middle of the US image in the lateral dimension (Fig. 4.3 (c)). Four laser diodes sequentially delivered four optical wavelengths of 740 nm, 780 nm, 808 nm and 830 nm to the tissue and the reflected light was detected by 10 optical fiber bundles which coupled detected light to 10 parallel

photomultiplier tube (PMT) detectors. The US transducer or probe was located in the middle and optical source and detector fibers were surrounding the US probe. The source powers measured at fiber tips were: 14-18mW (740nm), 17-23 mW (780nm), 17-23 mW (808nm) and 24-28 mW (830nm). The wavelengths 785 nm, 808 nm and 830 nm are used often in DOS and DOT systems (see Table 4.1) because of the need for deep tissue penetration. 740 nm provides more robust estimation of de-oxygenated hemoglobin in the NIR spectrum.

The measurement procedure and geometry of the US probe and optical source and detector fibers is shown in Fig. 4.3 (a) and (b). The co-registered hybrid probe was placed on a lesion first and 4 to 6 measurements were taken. Then, the probe was placed on the contralateral mirror position of the lesion, which was used as reference, and 4 to 5 measurements were taken. Background tissue μ_a and μ_s' were fitted from the reflectance measurements made at the contralateral normal breast as discussed in 4.1.1 [52]. For each wavelength, the absorption μ_a and reduced scattering coefficients μ_s' are fitted by eq. 4.5-4.6. [52].

The average μ_a and μ_s' obtained from 4-5 measurements made at the contralateral breast were used to characterize each patient's background tissue optical properties. Reconstruction of an absorption (μ_a) map of a lesion at each wavelength is based on the Born approximation and conjugate gradient search for optimization [78]. The tHb map of a lesion was directly computed by summation of HbO_2 and Hb from reconstructed μ_a maps given from eq. 1.1 [4].

For each lesion, the average of maximum values of 4 to 6 computed tHb maps was used to characterize the lesion. Bulk tissue or background tissue tHb concentration was calculated from fitted μ_a values at four optical wavelengths. To minimize the chest wall effect, the lesion tHb was subtracted by background hemoglobin level, which represents a relative tHb concentration.

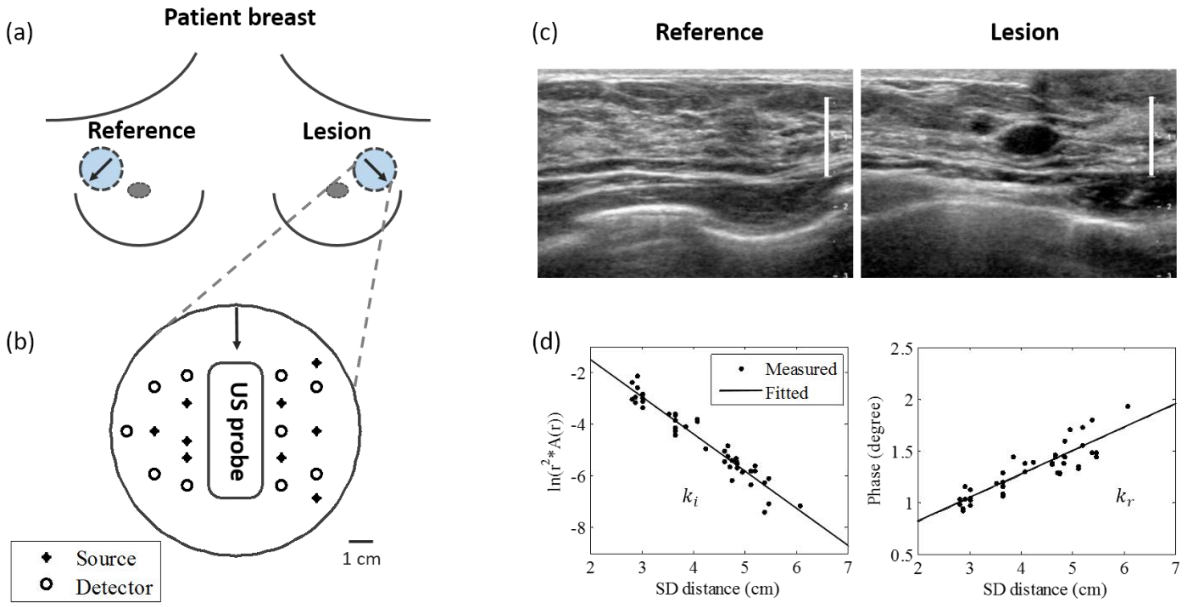

Figure 4.3. Measurement procedure (a) and geometry (b). (c) Typical co-registered ultrasound image taken at a normal breast (left) and lesion breast (right). Scale bars indicate 1 cm. (d) Reference measurement at 780 nm, amplitude (logarithmic scale, left) and phase (right) verses source and detector distance.

4.2.3 Chest wall depth detection

We defined chest wall depth as the distance from the skin to the top layer of chest wall muscle. An automated chest wall depth detection method was developed by one of our lab mates and applied to the co-registered US images. Briefly, detection of the chest wall is based on the fact that chest wall muscles appear as line structures in US images [88]. With that, Canny edge detection method was used generate the binary images, and then a Hough Transform based on structure segmentation using Gabor filter is applied to detect line structures. Finally, de-noising restrictions applied on the length, location and slope range are applied to automatically detect chest wall depth [89-95] .

In order to estimate the accuracy of this method, we measured the chest wall depth both by algorithm and manually by an experienced US breast imager, refereed as operator. We quantified the error by eq. 4.10 as:

$$Error = \frac{|Manual - Auto|}{Manual} \times 100\ \% \quad (4.10)$$

Empirically for cases with errors <15% which correspond to 2 to 4 mm for the average chest wall depth of 2 to 3 cm, we used automatically detected values. For cases with errors >15% the operator re-evaluated the chest wall depths and reassigned or confirmed the values.

4.2.4 Evaluation of diagnostic performance

Receiver operating characteristic (ROC) curve, as plot in Fig. 4.6, is a conventional way to evaluate the diagnostic performance of predictors (i.e., medical tests with positive/negative results) and select the optimal models in comparison with the true status of binary outcomes (i.e., cancer patients and non-cancer controls). ROC analysis has been widely applied in modern medicine, biometrics and many other fields related to diagnostic decision making. In statistics, a ROC curve is a graphical plot of true positive rate (TPR or sensitivity) against false positive rate (FPR or 1-specificity) at various threshold settings. Good prediction would yield a point toward the upper left corner of ROC space, and coordinate (0, 1) represents a perfect classification with 100% sensitivity (no false negatives) and 100% specificity (no false positives). The area under the curve (AUC), a summary statistics derived from ROC curve ranging from 0.5 to 1.0, is commonly considered as an effective measure of accuracy and a meaningful interpretation of ROC curve [96]. Many statistical methods have been developed to compare two ROCs from two diagnostic tests and evaluate statistical significance of either dissimilarities between two ROC curves or difference between two AUCs derived from ROC curves. In this study, ROC analysis was carried out by R package pROC [97], which offers a

helpful tool for visualizing, smoothing and comparing ROC curves, especially the paired design (diagnostic tests measured on same samples). The principle of ROC analysis has been described in the following section.

4.2.5 Statistical Analysis

Pearson correlation method was used to examine the correlations of the fitted μ_a and μ_s' with the chest wall depth. Two-sample t-test was also performed to compare the mean difference of tHb between the malignant group and each benign sub-group (Table 4.4, *p-values*). In order to evaluate the diagnostic performance of tHb levels in classification of malignant and benign lesions, the tHb levels were used as the predictor variable and the respond variable is a binary corresponding to the status of tumor diagnosis based on biopsy. For analysis #1, the respond variable is unity for early stage malignant tumors (Tis-T1) and zero for benign lesions; For analysis #2, respond variable is unity for all malignant tumors including Tis-T1 and late stage cancers (T2-T4) and zero for benign lesions. The false positive rate (1-specificity) and true positive rate (sensitivity) were computed in Matlab to generate ROC curves. In each ROC plot, the AUC and the corresponding 95% confidence interval were calculated using R package pROC [97]. The statistical difference of ROCs with and without subtracting background was evaluated by two tests in pROC: 1) the Venkatraman's test on two ROC curves; and 2) the bootstrap test on AUCs as opposed to the actual ROC curves. The Venkatraman's method evaluates the integrated absolute difference between ROCs at all operating points with a test statistics (corresponding to statistics *E* in pROC), whose null distribution is generated by permuting the pooled ranks of two predictor variables within a study subject [98]. In our study, the permutation was executed for 2,000 times as a default. The Bootstrapping method tests the equality of AUCs for two diagnosis [97]. It defines a statistics *D* by dividing difference of the

original two AUCs with a standard deviation (*s*), which is the standard deviation of AUCs difference and is computed with 2,000 times of bootstrap replicates. In each replicate, original diagnostic measurements are resampled with replacement. As the statistics *D* follows a normal distribution, *p*-value is calculated based on observed *D* score. For both tests, *p*-value was computed by a two-tailed paired test and statistical significance was considered at $p < 0.05$.

4.3 Results

We compared operator manually and algorithm automatically detected chest wall depths. Using an error measure defined in eq. 4.10, the percentage of cases with error <15% was 67%. For cases with error > 15% (33%), the operator re-evaluated the chest wall depths and reassigned or confirmed the values. Of all cases, an average algorithm detection error was 14%, which corresponds to 2 to 4 mm for the average chest wall depth of 2 to 3 cm.

We then analyzed the correlation between fitted background μ_a and μ_s' and the chest wall depth of the reference side which does not have known lesions at the time of the study based on the evaluations of the attending radiologists from available mammograms, US, and or magnetic resonance imaging (MRI). The fitted μ_a and μ_s' at four optical wavelengths are correlated with the chest wall depth as shown in Fig. 4.4 and Table 4.2 with *p-values* less than 0.0001. At each wavelength, the fitted μ_a has a much higher correlation coefficient than that of fitted μ_s'. Analysis of different races shows that as the skin color is getting lighter (the skin color was based on patient's race disclosed at the time of the consent), the correlation coefficient between μ_a and the chest wall depth is higher, while the correlation between μ_s' and the chest wall depth does not change much with skin color. This is likely caused by the deeper penetration of the diffused light when the skin color is lighter. There is no significant difference of chest wall depth between the white and black race groups and between the white and Asian

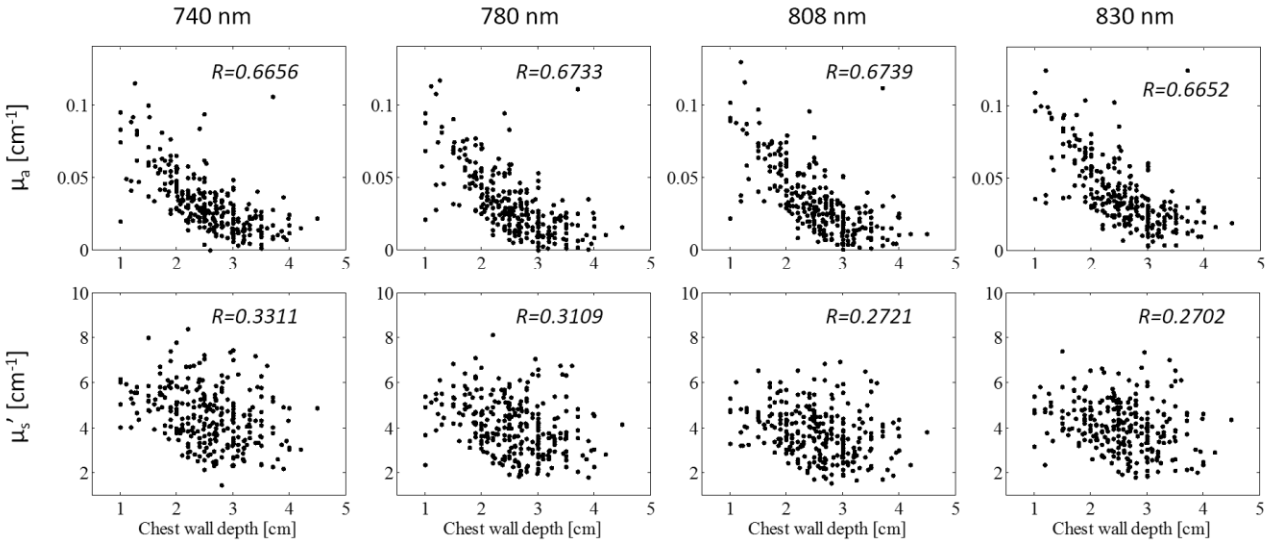

Figure 4.4. Fitted μ_a and μ_s' vs. chest wall depth at different wavelengths measured at normal reference side.

Table 4.2. Correlation coefficient (r) between fitted μ_a and μ_s' with chest wall depth of entire population and different races (Total N=303, Black N=48, Asian & Hispanic N=50, White N=144)

Background properties	Race	Chest wall depth (cm)	Wavelength			
			740 nm	780 nm	808 nm	830 nm
μ_a (cm^{-1})	All Patients	2.57±0.66	0.6656	0.6733	0.6739	0.6652
	Black	2.58±0.68	0.6998	0.7164	0.7046	0.6593
	Asian & Hispanic	2.49±0.70	0.6777	0.6594	0.6765	0.6596
	White	2.53±0.62	0.7752	0.7773	0.7800	0.7803
μ_s' (cm^{-1})	All Patients	2.57±0.66	0.3311	0.3109	0.2721	0.2702
	Black	2.58±0.68	0.2972	0.3203	0.1975	0.2022
	Asian & Hispanic	2.49±0.70	0.1746	0.2223	0.0927	0.2727
	White	2.53±0.62	0.3845	0.3389	0.3719	0.3213

Table 4.3. Breast tissue bulk optical properties (Mean ± Std) measured at four optical wavelengths of entire population and different races (Total N=303, Black N=48, Asian & Hispanic N=50, White N=144)

Background properties	Race	Chest wall depth (cm)	Wavelength			
			740 nm	780 nm	808 nm	830 nm
μ_a (cm^{-1})	All Patients	2.57±0.66	0.033±0.020	0.032±0.022	0.034±0.023	0.039±0.023
	Black	2.58±0.68	0.034±0.022	0.033±0.022	0.034±0.023	0.039±0.025
	Asian & Hispanic	2.49±0.70	0.035±0.020	0.036±0.025	0.039±0.027	0.042±0.027
	White	2.53±0.62	0.033±0.020	0.032±0.022	0.034±0.022	0.039±0.022
μ_s'(cm^{-1})	All Patients	2.57±0.66	4.5±1.3	4.1±1.2	3.7±1.1	4.6±1.1
	Black	2.58±0.68	4.7±1.6	4.4±1.4	4.0±1.3	4.2±1.3
	Asian & Hispanic	2.49±0.70	4.6±1.3	4.1±1.2	3.8±1.1	4.1±1.1
	White	2.53±0.62	4.5±1.2	4.0±1.2	3.7±1.1	4.1±1.1

& Hispanic groups, however, the correlation coefficients at four wavelengths for the white group is significantly larger than the black (p=0.0055) and Asian & Hispanic groups (p=0.0001), but no significant difference was found on the correlation coefficients between the black and Asian & Hispanic groups (p=0.1096). Table 4.3 shows the fitted μ_a and μ_s' values of the entire population and different races**.** No significant difference of μ_a or μ_s' was found between any two racial groups.

We further calculated the hemoglobin concentrations from fitted bulk tissue μ_as at four wavelengths. The correlation coefficients (r) and *p-values* between chest wall depth and computed background hemoglobin values were, tHb: $r = 0.6775$, $p < 0.0001$; HbO_2: $r = 0.6134$, $p < 0.0001$; and Hb: $r = 0.6017$, $p < 0.0001$, which are statistically significant.

We have shown in the previous study that the lesion maximum hemoglobin concentration can be used to differentiate benign from malignant lesions [79]. We have investigated the

improvement of using this method in differentiating benign and malignant lesions by subtracting the corresponding background hemoglobin concentration. Fig. 4.5 shows the differences without and with subtraction of the corresponding background from each patient between malignant group (both Tis-T1 and T2-T4) and benign sub-groups of Prolif., FA, FN, FC, Cyst and LN. Numerical differences, standard deviations (Std) and *p-values* were computed between malignant and benign sub-groups (except for Tissue and LN group due to small sample sizes) and shown in Table 4.4. The error bars in Fig. 4.5 and Std values in Table 4.4 indicate the standard deviations of the difference between malignant group and each benign sub-group. They were computed using the Stds and sample sizes (*n*) of two groups under comparison as $\text{Std} = \sqrt{\frac{Std1^2}{n1} + \frac{Std2^2}{n2}}$. An increased difference was found between the malignant group and 6 of the 7 benign groups in a range of 2-7 μM, except for the tissue & other benign group, which has a small sample size. The largest difference after subtraction was found from fibroadenoma (FA) due to the relative young patients with dense breast tissue and

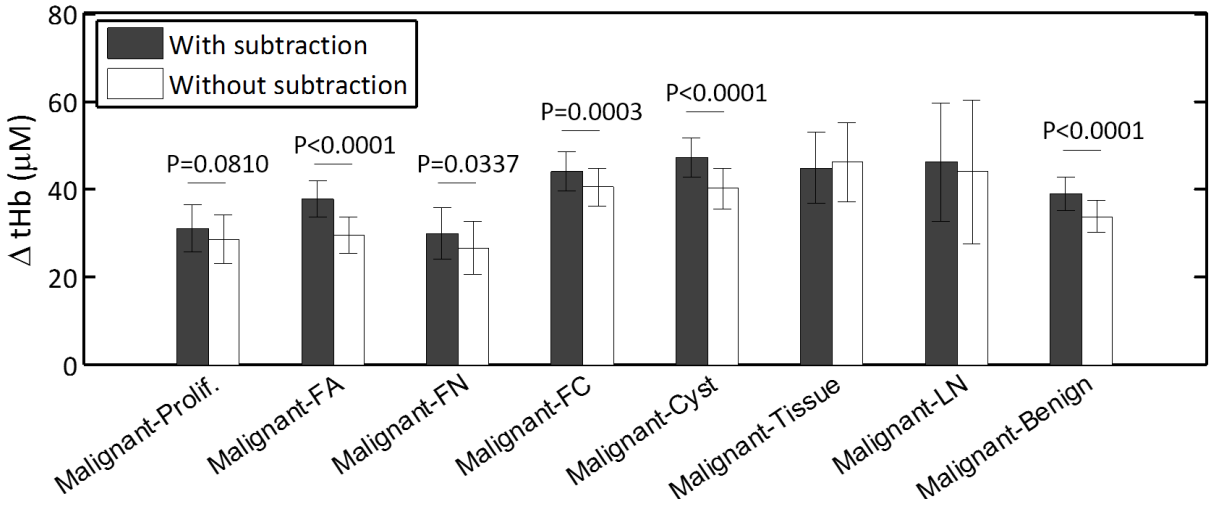

Figure 4.5. Total hemoglobin difference (ΔtHb) and Std between the malignant group (n=59) and benign sub-groups (Prolif. n=33, FA n=75, FN n=29, FC n=44, Cyst n=38, Tissue & other benign n=7 and LN n=6), and all benign group (n=232).

Table 4.4. Total hemoglobin differences (δ tHb), standard deviations (Std) and p-values *between the malignant and benign tumor sub-groups with and without subtracting the background*

Subtract -ion bg.	Comp. values	Prolif.	FA	FN	FC	Cyst	Tissue & others	LN	Benign
With	**ΔtHb**	30.9	37.6	29.8	43.9	47.1	44.6	46.0	38.9
	Std	5.5	4.2	5.9	4.5	4.4	8.1	13.6	3.7
	p-value	<0.0001	<0.0001	<0.0001	<0.0001	<0.0001	0.0004	0.0159	<0.0001
Without	**ΔtHb**	28.5	29.4	26.4	40.3	40.0	46.0	43.9	33.6
	Std	5.5	4.1	6.0	4.4	4.6	9.1	16.3	3.6
	p-value	<0.0001	<0.0001	0.0001	<0.0001	<0.0001	0.0011	0.0396	<0.0001

a shallower chest wall depth in this group (Mean ages are: 55±13, 41±12, 55±18, 49±12, 49±11, 51±13 and 47±14 years for Prolif., FA, FN, FC, Cyst, tissue & other benign and LN, respectively). And their average chest wall depths were: 2.64±0.54, 2.44±0.75, 2.53±0.70, 2.59±0.72, 2.42±0.62, 2.71±0.48 and 2.49±0.67 cm, respectively.

The ROC curves (sensitivity *vs.* 1-specificity) using a threshold of tHb level for predicting early stage malignant lesions (Tis-T1) and all malignant lesions (Tis-T1 and T2-T4) from the benign cases are given in Fig. 4.6. 64 μM was chosen as the optimal threshold for diagnosis using relative lesion tHb after subtracting the background values, and 80 μM was used for diagnosis without subtracting background values. We compared both ROCs and AUCs in R package pROC [97] using tHb levels before and after subtracting the background. When comparing the ROC curve after background subtraction against the one before subtraction, we obtained $p = 0.0025$ for Tis-T1 diagnosis and $p = 0.1010$ for all malignant lesion diagnosis. As shown in Fig. 4.6, we observed a significantly higher AUC for Tis-T1 diagnosis with an increased AUC of 3.0% ($p = 0.0016$) and all malignant lesion diagnosis with an increased AUC

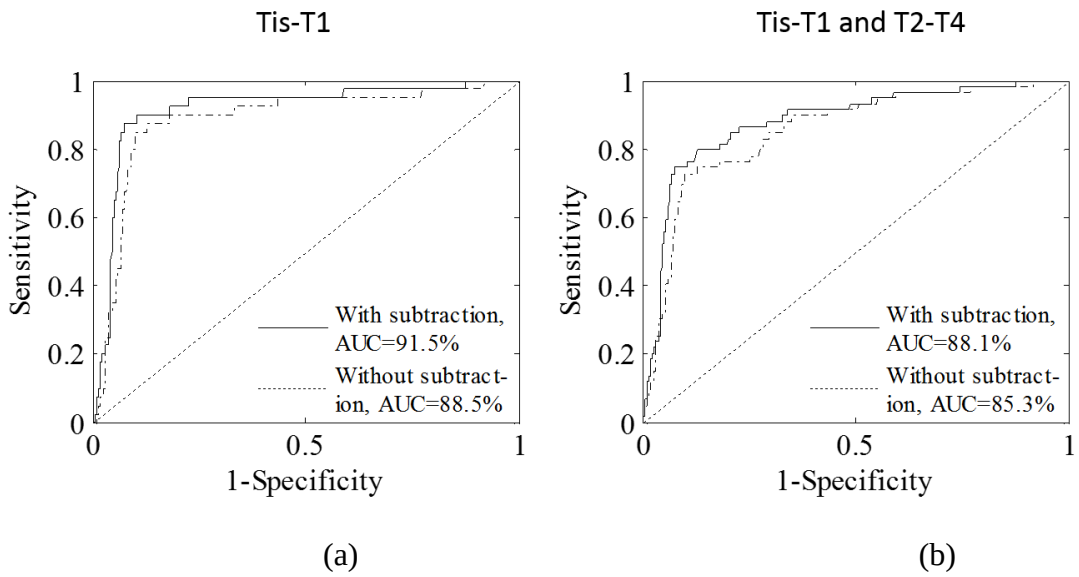

(a) (b)

Figure 4.6. ROC curve (a) Tis-T1 vs. benign cases and (b) Tis-T1 and T2-T4 vs. benign cases.

Table 4.5. Sensitivity, Specificity, Positive predictive value (PPV) and Negative Predictive Value (NPV) of tHb before (th=80 µM) and after (th=64 µM) subtracting background value

Subtraction bg.	Parameter	Sensitivity	Specificity	PPV	NPV
With	Tis-T1	87.5 %	92.6 %	66.0 %	97.8 %
	Tis-T1 and T2-T4	74.6 %	92.6 %	71.0 %	93.8 %
Without	Tis-T1	85.0 %	90.2 %	58.6 %	97.4 %
	Tis-T1 and T2-T4	72.9 %	90.2 %	64.2 %	93.2%

of 2.8% (p = 0.0159). These results have demonstrated that background subtraction method has consistently improved diagnostic performance for early breast lesions.

Table 4.5 shows the sensitivity, specificity, positive predictive value (PPVs) and negative predictive value (NPVs) in diagnosing malignant tumor from the benign lesions using tHb data with and without subtracting the background data. Results show an improvement of 1.7-2.5%

in sensitivity and specificity, 6.8-7.4% improvement in PPV and around 0.4-0.6% improvement in NPV after subtracting the background values.

4.4 Discussion

The fitted μ_a and μ_s' measured in the reflection geometry using larger source and detector separations are not true representation of tissue background optical properties due to the influence of chest wall underneath the breast tissue. This suggests that diagnosis between malignant and benign lesions is best performed by using relative hemoglobin concentrations after subtracting corresponding background values computed from fitted μ_as at multiple optical wavelengths. Another advantage of using relative hemoglobin values for diagnosis is that this method eliminates the effect due to hemoglobin level fluctuations in certain type of patients who may be under anemia or some drug effect. For those patients, the background blood hemoglobin concentration differs significantly from the normal values. Skin color does affect the light penetration and therefore the fitted background values from dark skin color patients are less affected by the chest wall depth. We understood that there is individual difference of skin color from each race group, however, our assumption that the skin color order from dark to light: black>Asian & Hispanic>white, was based on the general trend and our result shows an agreement with this trend. The Asian & Hispanic group has a mixed skin color, and no significant difference on the correlation of fitted μ_a with chest wall depth was found compared with the black group. The sample size of each group is large and it should not affect reported results. As shown in Table 4.3, the fitted μ_a and μ_s' for the three groups are very similar.

For each patient, we typically collect 4 to 6 sets of measurements from the contralateral breast at slightly different locations. The separation between each set of measurements varies from few seconds to tens of seconds because of hand-held operation. The fitted background

tHb of each patient is the average of these 4 to 6 data sets. In general, the fitted tHbs for each patient are very close with average standard deviation of 2.0 μM.

The relative tHb computed with reconstructed μ_a was used as the predictor for generating ROC curves for the study. When comparing the closeness of two ROC curves with and without background subtraction by the Venkatraman's method in R package pROC, we observed a statistically different ROC curves for Tis-T1 diagnosis (p = 0.0025) but similar ROC curves for all malignant lesion diagnosis (p = 0.1010). Consistent with this, the background subtraction method yielded a statistically higher AUC for Tis-T1 diagnosis (p = 0.0016, Fig. 4.6a). However, we also obtained a higher AUC for all malignant lesion diagnosis (p = 0.0159, Fig. 4.6b). The inconsistent result is likely due to differential statistics employed in two different ROC tests. As can be seen in either case of Fig. 4.6, the 95% CIs of two AUCs with and without subtracting background overlap with each other. In general, if confidence intervals do not overlap, it suggests a significant conclusion, however the reverse is not always true and our data might be this case. Given the observed difference of two AUCs (Tis-T1 diagnosis: 3%; all malignant lesion diagnosis: 2.8%), the 2,000 times of bootstrap resampling method generated small empirical standard deviations, for Tis-T1 diagnosis and for all malignant cases, resulting in large D values and significant p-values accordingly. Nevertheless, improvement of our subtracting method for all malignant lesion diagnosis can only be considered as marginal and needs to be confirmed by future studies.

We also studied the distribution of tHb versus age, and found the trend was generally in agreement with that reported by Cerussi *et al* [65]. However, our data were more scattered than the results reported in this paper. The chest wall effect still played a role on our data even we selected measurements with the chest wall depth deeper than 2 cm. Moreover, as shown in

Table 4.1, the measured μ_a is in the range of 0.025-0.110 cm^{-1} and μ_s' in the range of 5.0-15.5 cm^{-1}, while our measured μ_a is in the range of 0.0001-0.130cm^{-1} and μ_s' in the range of 0.6-8.4 cm^{-1}. Although μ_a is similar to the reported values, μ_s' is lower. The tHb values were measured to be in the range of 1-58 μM, which is similar to the range of 0-60 μM reported in Ref. [65], and lower than the range of 10-90 μM reported in Ref. [99].

In the past, we also tried to remove the chest wall effect by using shorter source-detector measurements [80, 82-84]. Results show that although correlation coefficient was smaller when shorter source-detector measurements were selected, the fitted μ_a was still correlated with the chest wall depth but not μ_s' for the source and detector range we have.

4.5 Conclusion

This chapter reviewed breast tissue optical properties measured by diffuse optical spectroscopy or tomography techniques. Our measurements from 297 patients show significant correlation between the measured optical properties and the chest wall depth even the background μ_a were similar to those reported in the literature. By subtracting background tHb computed from fitted background μ_as of all wavelengths, the relative tHb improves sensitivity, specificity, positive and negative predictive values in breast cancer diagnosis.

Chapter 5 Hemoglobin optical phantom

5.1 Introduction

5.1.1 Tissue mimicking phantom

In our previous studies, we generally used 0.8% intralipid solution as a phantom mimicking the optical properties of background normal breast tissue for calibrating the DOT system. Since the aqueous suspension is not easy to handle with and need to be prepared every time before experiment, we started to make a solid phantom with the RTV (room temperature vulcanization silicone) silicon rubber, whose preparation procedures is described in Appendix II.

In order to simulate the diseased tissue (the target, i.e. tumor) embedded in normal background, we first used different sized and different contrast spherical balls (phantoms made in our lab by materials calibrated with DOT system) and then cubes (made with ink, TiO_2 and RTV materials), whose absorption at the NIR wavelength range were made to be close to 0.1 cm^{-1} and 0.2 cm^{-1}. But these phantoms cannot be used to simulate the SO_2 property of diseased tissue. Later for the evaluation of SO_2 measurement accuracy by our DOT system, we made a hemoglobin filled glass ball phantom to closely mimic the enriched blood supply in the tumor. The oxygen saturation can be carefully manipulated to be close to 100% and 0% for the measurement.

5.1.2 Hemoglobin

Hemoglobin (Hb) is the main absorber in blood (Fig. 5.1). It also functions in transporting the oxygen in the human body. The combination of Hb with oxygen or other molecules (such as CO or CO_2) changes its absorption spectrum in both visible and near infrared (Fig. 5.2) wavelength range. Therefore, by measuring the multi-wavelength absorption map with a DOT system, it is possible to monitor the SO_2, which equals to the percent of HbO_2 over tHb, in the

investigated tissue *in vivo*. In order to estimate the accuracy of the measurement by DOT system and also to calibrate the system, making a phantom that mimic the blood optical properties with known SO_2 levels and time-stable properties is in need.

In selecting hemoglobin product that can be used for making a phantom, the absorption spectrum of hemoglobin from human and animal is of little difference. However, the ferrous state hemoglobin (with Fe2+ in the center of the heme, Fig. 5.1) is easily transformed into the methemoglobin in the air, which is the ferric state (Fe3+) and lose its combining capability to O_2, whose extinction coefficient spectrum gradually changes to the methemoglobin one shwon in Fig. 5.2. An empirical estimation of the speed of this process is that approximately 1% HbO_2 changes into methemoglobin per day at about 0°C in liquid solution. Therefore, it is critical to avoid or reduce contact of hemoglobin with the omnipresent oxygen in air in storing and in making a phantom.

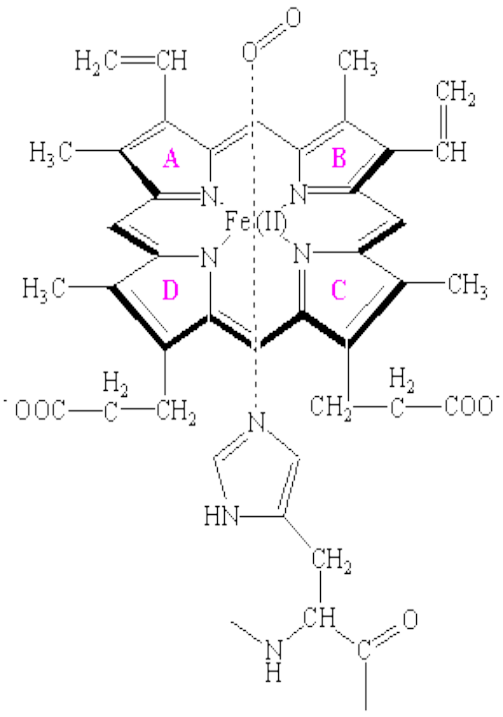

Figure 5.1. Molecular structure of the heme in hemoglobin [104]

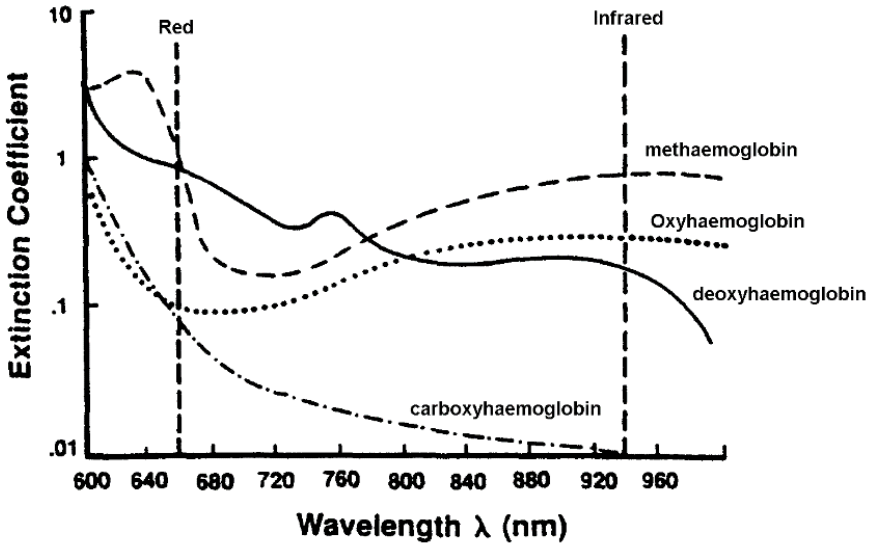

Figure 5.2. Extinction coefficient of different state of Hb [105]

5.1.3 Deoxygenation of hemoglobin

At the beginning of this study, three methods were considered for launching the deoxygenation process: by pumping nitrogen gas [100], by adding yeast and then pumping nitrogen gas [101], or by adding sodium dithionite ($Na_2S_2O_4$) [102]. We have tried with all three methods. Unfortunately, the first and second methods was not seen as apparent effective. The third method was observed to deoxygenate the hemoglobin solution quickly, but the deoxygenated hemoglobin was not stable and can change within minutes. According to literature, releasing of O_2 by blood hemoglobin after mixing with $Na_2S_2O_4$ was found and studied for long [102]. The reaction is fast and product is not stable as it is quickly re-oxygenated probably, possibly resulted from the reaction of some side-products from the initial reduction. The reductive half-time is not linear with $Na_2S_2O_4$ concentration. For blood cells, when the concentration increases to around 25 mM, the O_2 releasing half-time is approaching flat [102].

5.2 Materials and methods

For later phantom experiment, as Instrumentation Laboratory provides standard Hb solution with the tHb concentration similar to that of human and known SO_2 [103], we used this type (Multi-4, Level 2, Instrumentation Laboratory, MA) as the initial HbO_2 sample and material for making the deoxygenated Hb sample. According to the specifications provided by company, for Multi-4, Level 2 product the hemoglobin concentration is: tHb=138 g/L, and HbO_2 is around 96.6%.

We used the UV-Vis spectrometer (Varian Cary®, Agilent, US) and disposable cuvette for the calibration of hemoglobin concentration and SO_2. After that, a series of tests using the DOT system were made. For each measurement, we filled a thin wall glass ball (thickness ~0.1 cm) with diluted HbO_2 or Hb solution, sealed the ball neck with hot glue and connected the ball with clear glass fibers. The ball and fiber are then fixed to the clay attaching to the bottom of the container. The aqueous background matrix was then filled in the container and during experiment, the DOT probe surface is immersed in the background matrix and can be adjusted up and down to acquire data with probe-to-target-top distance varying between 1 to 3 cm, with 0.5 cm step increments. The background matrix was prepared with different concentration of intralipid in water.

During the experiment, we followed three steps of measurement: First, we tested with target filled by different hemoglobin concentration solutions (100 and 180 μM) with background medium (background II, 0.8% intralipid by volume, and μ_a=0.02-0.03 cm^{-1} and μ_s'=8-9 cm^{-1}). We measured with different sized glass balls (d=2.0 cm, 2.4 cm and 2.8 cm) and at various depths (1.5 cm, 2.0 cm, 2.5 cm, 3.0 cm and 3.5 cm). Secondly, we changed the background properties to μ_a=0.005-0.02 cm^{-1}, μ_s'=3-4 cm^{-1} (background I, 0.4% intralipid) and

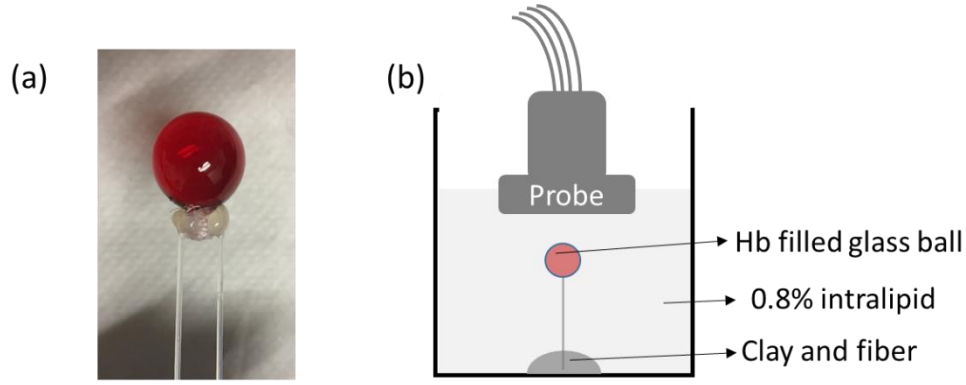

Figure 5.3. (a) Glass ball filled with HbO2 solution and connected to holding fibers, and (b) Sketch of the testing experimental setup.

μ_a=0.02-0.03 cm^{-1}, μ_s'=11-12 cm^{-1} (background III, 1.2% intralipid) and repeated previous procedures. Third, we acquired DOT data at 180 μM HbO_2 and Hb solution and with background II. The procedures in preparing Hb solution can be referred to Appendix IV. We then computed the SO_2 with different wavelength measurements at 740 nm, 780 nm, 808 nm and 830 nm and compared with calibrated values by the spectrometer.

DOT images are reconstructed from measured data and the maximum reconstructed μ_a will be compared with the calibrated values. The HbO_2 and Hb concentrations are computed with method described in part 1.4 using reconstructed peak absorption coefficients at 740, 780, 808 and 830 nm. When computing the SO_2 for some HbO_2 samples, the results are slightly higher than 100%, and we assume this is due to computation error and correct them as 100% in later results description. We tested the target SO_2 with different glass ball sizes, different depths, different backgrounds and different calibrated SO_2 (0% and 100%).

5.3 Results

5.3.1 Calibration result

The calibration results (spectra and computed SO_2) measured with the UV-Vis spectrometer are displayed in Fig. 5.6 and Table 5.4. Fig. 5.6 show the plots of average spectra of oxygenated

and de-oxygenated Hb solutions generated and measured 5 times at 180 μM concentration. Hb solution was generated by adding 50 mg $Na_2S_2O_4$ to the 4 ml solution (resulting in 72 mM concentration). The calculated SO_2 for each measurement are listed in Table 5.4.

5.3.2 Results of different concentration, different size, different background medium

With the HbO_2 solution diluted at 100 and 180 μM, the measured and reconstructed μ_as are shown in Table 5.1, and the SO_2 from 3 cm target depth measurements (from the result at these concentrations measurements at 3-3.5 cm are more accurate) are shown in Table 5.2. Theoretically, the SO_2 for this solution should be 96-100%, as indicated by the product specification and it should not decrease in short time with air presence.

Table 5.1. Reconstructed μ_a measured at 100 μM and 180 μM

Target diameter (cm)	**λ (nm)**	**Background I**		**Background II**		**Background III**	
		100 μM	**180 μM**	**100 μM**	**180 μM**	**100 μM**	**180 μM**
2.0	**740**	0.020	0.027	0.035	0.039	0.045	0.048
	780	0.041	0.064	0.053	0.064	0.063	0.068
	808	0.050	0.078	0.062	0.073	0.081	0.081
	830	0.061	0.107	0.074	0.091	0.091	0.080
2.4	**740**	0.019	0.026	0.054	0.040	0.045	0.050
	780	0.045	0.065	0.068	0.082	0.065	0.088
	808	0.048	0.082	0.064	0.095	0.062	0.106
	830	0.060	0.137	0.086	0.110	0.058	0.114
2.8	**740**	0.020	0.026	0.038	0.043	0.039	0.061
	780	0.041	0.047	0.056	0.085	0.068	0.080
	808	0.045	0.065	0.059	0.096	0.084	0.078
	830	0.063	0.098	0.070	0.111	0.075	0.085

Table 5.2. SO_2 (%) measured at 100 μM and 180 μM

Target diameter (cm)	Background I		Background II		Background III	
	100 μM	**180 μM**	**100 μM**	**180 μM**	**100 μM**	**180 μM**
2.0	100	100	92	97	93	82
2.4	100	100	71	100	62	93
2.8	100	100	83	100	90	66

The parameters set in processing the data are: For 2.0 cm diameter target, fine mesh x, y and z axis radius are set as 2.7 cm, 2.7 cm and 0.89 cm. For 2.4 cm diameter target, these are set as 3.3 cm, 3.3 cm and 1.09 cm. For 2.8 cm diameter target, these are set as 3.9 cm, 3.9 cm and 1.29 cm. The fine mesh pixel resolution is 0.25 cm in x and y axis, and 0.5 cm in z axis. The course mesh size is 9×9×3.5 cm in x, y and z axis, and its resolution is 1.5 cm in x and y axis, and 1 cm in z axis. In reconstruction, the target centers are slightly moved around to make the peak value to be close to fine mesh area center.

From the DOT result, although the reconstructed μ_a is much smaller than the theoretical values (for 100μM HbO_2 at 780 nm: theoretical μ_a = 0.164 /cm, with calculation procedures shown in Appendix III, and the calibrated results shown in Fig. 5.6; And for HbO_2 180 μM at 780 nm: theoretical μ_a = 0.294 /cm), the reconstructed values at different conditions show some trends: Target with 180 μM hemoglobin solution shows more accurate measured SO_2 result. At these concentrations, deeper target depth (3-3.5 cm) results in more accurate SO_2 result. Reconstructed μ_a are generally higher for stronger scattered background medium (background III), but the measured SO_2 is more accurate at less scattered medium (background I). The target size is not shown to have significant effect on the reconstructed value.

5.3.3 Oxy-Hb and deoxy-Hb measurement

As a result of the change of spectra after $Na_2S_2O_4$ is added, a visible color change of the solution is also shown (Fig. 5.4). Calibrated absorbance spectra measured by the UV-Vis spectrometer is shown in Fig. 5.6. And the measured absorption coefficients at 740, 780, 808 and 830 nm with the DOT system with target at 3 cm depth are shown in Fig. 5.5. Both are the average of measurements of 5 times. Note a difference of cross-point exists in the HbO_2 and Hb sample spectra between the DOT and spectrometer measurement.

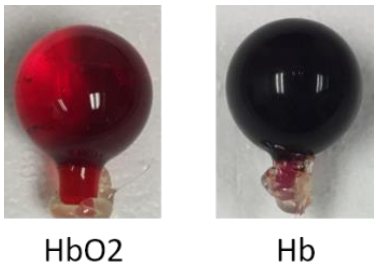

Figure 5.4. Photo of glass ball (2 cm) filled with hemoglobin samples

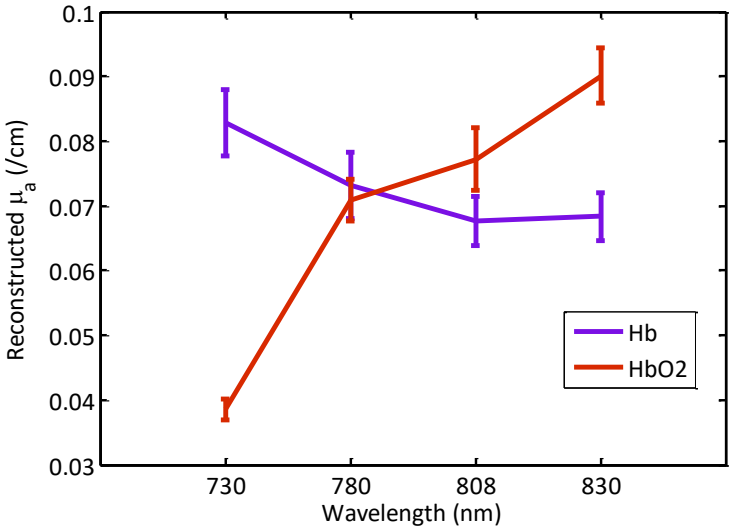

Figure 5.5. μ_a of hemoglobin samples measured with DOT system

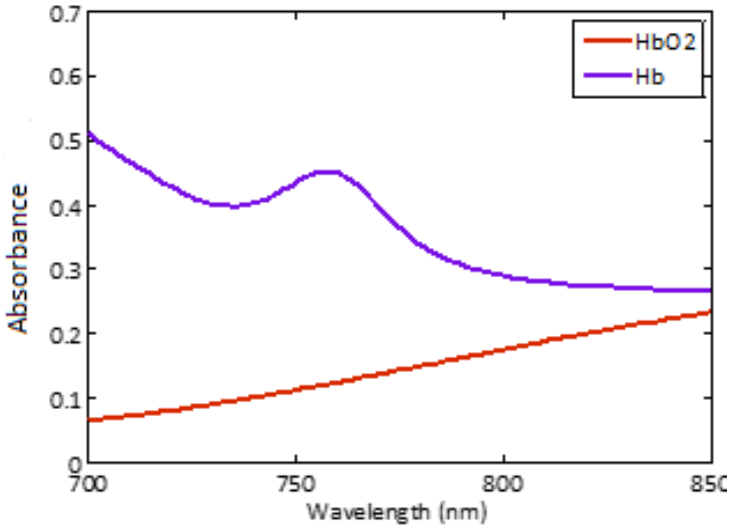

Figure 5.6. Absorbance of hemoglobin samples measured with spectrometer

Table 5 3. SO_2 (%) computed from the DOT measured data

Solution\Depth	1.5 cm	2 cm	2.5 cm	3 cm
HbO_2_1	45	48	77	96
HbO_2_2	30	44	68	98
HbO_2_3	44	75	64	93
HbO_2_4	77	76	71	97
HbO_2_5	36	49	75	94
Hb_1	82	93	22	21
Hb_2	59	85	32	26
Hb_3	52	68	45	26
Hb_4	67	83	33	28
Hb_5	49	76	41	27

Table 5.4. SO_2 (%) computed from the spectrometer measured data

HbO_2	97.8	97.5	97.4	96.7	97.3
Hb	6.6	5.3	13.4	6.0	4.3

The computed SO_2 from spectra are listed in Table 5.3 and 5.4. From the DOT data (Table 5.3), measurement with target at 3 cm depth gives more accurate SO_2 result, same as in 5.3.2. And by comparing DOT measurements with the calibrated data (Table 5.4), the SO_2 values measured from two systems with the HbO_2 sample are consistent, but measured SO_2 values of Hb sample by DOT system are ~20% higher than those measured by the spectrometer.

5.4 Discussion

In this study, the reconstructed μ_a from DOT data is much lower than the theoretical and calibrated values. We concede that the reflection due to thin wall of glass ball contributed a little on the error. Major part of this error should come from parameters setting for reconstruction, as reducing the fine mesh dimension and enlarging the fine voxel size leads to an overall higher reconstructed μ_a. In processing this study results, I used similar parameters setting that was used for processing clinical data. In order to get accurate reconstructed μ_a, this needs to be adjusted. However, the trend given by current results should not change, as same parameters are used for reconstruction at all cases for evaluating the effect of different target size, different target contrast and different background property.

From Fig. 5.6, the average measured spectrum of Hb sample was raised up significantly comparing that of the HbO_2 sample. This causes the moving of cross-point between the HbO_2 and Hb spectra at the same concentration (theoretically they should have cross point at ~800 nm). It can be explained as the result from increased scattering coefficients after adding $Na_2S_2O_4$. Since reflected signal is measured in DOT system and transmitted signal measured in the UV-Vis spectrometer, it results in decreased absorption measurements by DOT system, and increased absorbance measurements by the spectrometer.

Table 5.3 and 5.4 also show measured SO_2 difference between DOT data and the spectrometer measured data. The major reason should be operative timing difference. For spectrometer measurement, we used the cuvette as the hemoglobin container and can seal it with a stopper in seconds then measure immediately after adding $Na_2S_2O_4$. For DOT measurement, we injected sample into the glass ball with a syringe, sealed the ball with hot glue, fixed it into the intralipid by clay and fiber, adjusted the probe position and then started to measure. As the re-oxygenation of de-oxygenated hemoglobin after adding $Na_2S_2O_4$ occurs within minutes, we manipulated the temperature carefully to slow this process. We assumed and saw from the results that a low temperature slows the de-oxygenation process, and after the mixed solution being isolated from air, incubation at warm environment accelerates the de-oxygenation reaction and later re-oxygenation is retarded due to the isolation. This can be seen from Appendix IV calibration result, that after adding $Na_2S_2O_4$ and glass ball sealing, longer incubation time shows better results.

5.5 Conclusion

In summary, from this group of hemoglobin measurements, target with 180 μM HbO_2 solution shows more accurate measured SO_2. At 100 μM and 80 μM concentrations, measured SO_2 is better discernable and more stable when the target depth is at around 3 cm. Reconstructed μ_a are generally higher for more scattered background medium, but measured SO_2 is more accurate at less scattered medium. DOT system is confirmed to be able to measure HbO_2 and Hb sample with comparable results to the spectrometer ones.

Chapter 6. Summary and future works

6.1 Tumor hypoxia dyes

Tumor hypoxia is an important tumor microenvironment and targeting tumor hypoxia is significant in predicting tumor response to treatments. We did a series of *in vitro*, *in vivo* and *ex vivo* experiment and illustrated improved performance of the third generation hypoxia-targeting rigid dye in labeling mice tumor. The stained areas by our dye correlate with those stained by the commercial hypoxyprobe^{TM}-1. Further studies also showed the 4-nitroimidazole-ICG retained to a great extent in hypoxic tumors when compared with the second generation piperazine-2-nitroimidazole ICG.

Currently we are moving toward the understanding about the mechanism of our dyes staying more in the tumor, liver and kidney. Promising results have shown some protein(s) from the tumor extract that are bound by our dyes were found on the SDS-PAGE gel. Further experiment will be done in separating and purifying these protein(s) by using the biotin-avidin reaction and in obtaining the exact molecular structure of the protein(s). The toxicity of our 2-nitroimidazole dyes should also be investigated.

6.2 DOT breast cancer diagnosis

We analyzed the chest wall effect on the breast DOT data from 297 patients, and tested the effect of applying a direct subtracting method on reducing the chest wall effect. Results show solid improved prediction values in using the measured ΔtHb to detect early malignant tumor from investigated tumor lesions. Moreover, from the results we also found the chest wall effect on patient data with different skin colors is different. Despite the chest wall effect, a decreasing trend of hemoglobin values were shown with older ages of the patient. Lastly, a hemoglobin phantom that mimics the oxygen saturation property (0% and 100%) of breast lesion is made

and tested. Later study should towards the evaluation of adjusted reconstructing parameters setting on the accuracy of measured target properties (μ_a and SO_2). The property measurement error is also shown to be different at different depths. This problem is under investigation by one of our lab mates. A depth compensation algorithm or lookup table is to be developed for getting more similar reconstructed values at all depths.

References

[1] B. A. Kohler, R. L. Sherman, N. Howlader, A. Jemal, A. B. Ryerson, K. A. Henry, F. P. Boscoe, K. A. Cronin, A. Lake, and A.-M. Noone, "Annual report to the nation on the status of cancer, 1975-2011, featuring incidence of breast cancer subtypes by race/ethnicity, poverty, and state," Journal of the National Cancer Institute, vol. 107, p. djv048, 2015.

[2] B. J. Tromberg, B. W. Pogue, K. D. Paulsen, A. G. Yodh, D. A. Boas, and A. E. Cerussi, "Assessing the future of diffuse optical imaging technologies for breast cancer management," Medical physics, vol. 35, pp. 2443-2451, 2008.

[3] M. R. Hamblin and T. N. Demidova, "Mechanisms of low level light therapy," in Biomedical Optics 2006, 2006, pp. 614001-614001-12.

[4] S. Prahl, "Optical absorption of hemoglobin," Oregon Medical Laser Center, http://omlc. ogi. edu/spectra/hemoglobin/index. html, vol. 15, 1999.

[5] P. Vaupel and A. Mayer, "Hypoxia in cancer: significance and impact on clinical outcome," Cancer and Metastasis Reviews, vol. 26, pp. 225-239, 2007.

[6] M. C. Brahimi-Horn, J. Chiche, and J. Pouysségur, "Hypoxia and cancer," Journal of molecular medicine, vol. 85, pp. 1301-1307, 2007.

[7] P. Vaupel, F. Kallinowski, and P. Okunieff, "Blood flow, oxygen and nutrient supply, and metabolic microenvironment of human tumors: a review," Cancer research, vol. 49, pp. 6449-6465, 1989.

[8] J. M. Brown and W. R. Wilson, "Exploiting tumour hypoxia in cancer treatment," Nature Reviews Cancer, vol. 4, pp. 437-447, 2004.

[9] W. R. Wilson and M. P. Hay, "Targeting hypoxia in cancer therapy," Nature Reviews Cancer, vol. 11, pp. 393-410, 2011.

[10] M. Höckel and P. Vaupel, "Tumor hypoxia: definitions and current clinical, biologic, and molecular aspects," Journal of the National Cancer Institute, vol. 93, pp. 266-276, 2001.

[11] E. Hammond, M.-C. Asselin, D. Forster, J. P. O'Connor, J. Senra, and K. Williams, "The meaning, measurement and modification of hypoxia in the laboratory and the clinic," Clinical oncology, vol. 26, pp. 277-288, 2014.

[12] A. Nunn, K. Linder, and H. W. Strauss, "Nitroimidazoles and imaging hypoxia," European journal of nuclear medicine, vol. 22, pp. 265-280, 1995.

[13] L. Mei, Y. Wang, and T. Chu, "99m Tc/Re complexes bearing bisnitroimidazole or mononitroimidazole as potential bioreductive markers for tumor: synthesis, physicochemical characterization and biological evaluation," European journal of medicinal chemistry, vol. 58, pp. 50-63, 2012.

[14] H. Huang, H. Zhou, Z. Li, X. Wang, and T. Chu, "Effect of a second nitroimidazole redox centre on the accumulation of a hypoxia marker: synthesis and in vitro evaluation of 99m Tc-labeled bisnitroimidazole propylene amine oxime complexes," Bioorganic & medicinal chemistry letters, vol. 22, pp. 172-177, 2012.

[15] A. Bol, D. Labar, B. Jordan, J. Magat, L. Mignion, V. Grégoire, and B. Gallez, "Hypoxia imaging with the nitroimidazole 18 F-FAZA PET tracer: a comparison with OxyLite, EPR oximetry and 19 F-MRI relaxometry," Radiotherapy and Oncology, vol. 105, pp. 29-35, 2012.

[16] Z. Li and T. Chu, "Recent advances on radionuclide labeled hypoxia-imaging agents," Current pharmaceutical design, vol. 18, pp. 1084-1097, 2012.

[17] Z. Guo, S. Park, J. Yoon, and I. Shin, "Recent progress in the development of near-infrared fluorescent probes for bioimaging applications," Chemical Society Reviews, vol. 43, pp. 16-29, 2014.

[18] A. Corlu, R. Choe, T. Durduran, M. A. Rosen, M. Schweiger, S. R. Arridge, M. D. Schnall, and A. G. Yodh, "Three-dimensional in vivo fluorescence diffuse optical tomography of breast cancer in humans," Optics express, vol. 15, pp. 6696-6716, 2007.

[19] M. Aldrich, C. Davies-Venn, B. Angermiller, H. Robinson, W. Chan, S. Kwon, and E. Sevick-Muraca, "Concentration of indocyanine green does not significantly influence lymphatic function as assessed by near-infrared imaging," Lymphatic research and biology, vol. 10, pp. 20-24, 2012.

[20] C. Pavlik, N. C. Biswal, F. C. Gaenzler, M. D. Morton, L. T. Kuhn, K. P. Claffey, Q. Zhu, and M. B. Smith, "Synthesis and fluorescent characteristics of imidazole–indocyanine green conjugates," Dyes and Pigments, vol. 89, pp. 9-15, 2011.

[21] N. Nijegorodov and W. Downey, "The influence of planarity and rigidity on the absorption and fluorescence parameters and intersystem crossing rate-constant in aromatic-molecules," Journal of physical chemistry, vol. 98, pp. 5639-5643, 1994.

[22] H. Suzuki, "Relations between electronic absorption spectra and spatial configurations of conjugated systems. I. Biphenyl," Bulletin of the Chemical Society of Japan, vol. 32, pp. 1340-1350, 1959.

[23] I. Mohammad, C. Stanford, M. D. Morton, Q. Zhu, and M. B. Smith, "Structurally modified indocyanine green dyes. Modification of the polyene linker," Dyes and Pigments, vol. 99, pp. 275-283, 2013.

[24] B. W. Pogue and M. S. Patterson, "Review of tissue simulating phantoms for optical spectroscopy, imaging and dosimetry," Journal of biomedical optics, vol. 11, pp. 041102-041102-16, 2006.

[25] N. C. Biswal, C. Pavlik, M. B. Smith, A. Aguirre, Y. Xu, S. Zanganeh, L. T. Kuhn, K. P. Claffey, and Q. Zhu, "Imaging tumor hypoxia by near-infrared fluorescence tomography," Journal of biomedical optics, vol. 16, pp. 066009-066009-8, 2011.

[26] Y. Xu, S. Zanganeh, I. Mohammad, A. Aguirre, T. Wang, Y. Yang, L. Kuhn, M. B. Smith, and Q. Zhu, "Targeting tumor hypoxia with 2-nitroimidazole-indocyanine green dye conjugates," Journal of biomedical optics, vol. 18, pp. 066009-066009, 2013.

[27] S. Zanganeh, F. Zhou, A. Abuteen, I. Mohammad, M. Smith, and Q. Zhu, "Biodistribution study of 2-nitroimidazole indocyanine green conjugate dye conjugates," in Biomedical Optics, 2014, p. BT3A. 51.

[28] A. Abuteen, F. Zhou, C. Dietz, I. Mohammad, M. B. Smith, and Q. Zhu, "Synthesis of a 4-nitroimidazole indocyanine dye-conjugate and imaging of tumor hypoxia in BALB/c tumor-bearing female mice," Dyes and Pigments, vol. 126, pp. 251-260, 2016.

[29] F. Zhou, A. Abuteen, C. Dietz, I. Mohammad, M. Smith, and Q. Zhu, "Imaging of Tumor Hypoxia using 4-Nitroimidazole ICG-conjugate," in Optical Tomography and Spectroscopy, 2016, p. JM3A. 54.

[30] S. Kizaka‐Kondoh and H. Konse‐Nagasawa, "Significance of nitroimidazole compounds and hypoxia‐inducible factor‐1 for imaging tumor hypoxia," Cancer science, vol. 100, pp. 1366-1373, 2009.

[31] P. Chan, K. Skov, and B. James, "Further studies on toxic and radiosensitizing properties of ruthenium complexes of 4-nitroimidazoles," International Journal of Radiation Biology and Related Studies in Physics, Chemistry and Medicine, vol. 52, pp. 49-55, 1987.

[32] Z. Li, J. Zhang, Z. Jin, W. Zhang, and Y. Zhang, "Synthesis and biodistribution of novel 99m Tc labeled 4-nitroimidazole dithiocarbamate complexes as potential agents to target tumor hypoxia," MedChemComm, vol. 6, pp. 1143-1148, 2015.

[33] F. Zhou, S. Zanganeh, I. Mohammad, C. Dietz, A. Abuteen, M. B. Smith, and Q. Zhu, "Targeting tumor hypoxia: a third generation 2-nitroimidazole-indocyanine dye-conjugate with improved fluorescent yield," Organic & Biomolecular Chemistry, vol. 13, pp. 11220-11227, 2015.

[34] M. Grabolle, M. Spieles, V. Lesnyak, N. Gaponik, A. Eychmüller, and U. Resch-Genger, "Determination of the fluorescence quantum yield of quantum dots: suitable procedures and achievable uncertainties," Analytical Chemistry, vol. 81, pp. 6285-6294, 2009.

[35] M. Eyal, R. Gvishi, and R. Reisfeld, "SPECTROSCOPIE OF LASER DYE OXAZINE-170 AS A FUNCTION OF ENVIRONMENT AND pH," Le Journal de Physique Colloques, vol. 48, pp. C7-471-C7-473, 1987.

[36] S. K. Cool, K. Breyne, E. Meyer, S. C. De Smedt, and N. N. Sanders, "Comparison of in vivo optical systems for bioluminescence and fluorescence imaging," Journal of fluorescence, vol. 23, pp. 909-920, 2013.

[37] O. Mazuryk, M. Maciuszek, G. Stochel, F. Suzenet, and M. Brindell, "2-Nitroimidazole-ruthenium polypyridyl complex as a new conjugate for cancer treatment and visualization," Journal of inorganic biochemistry, vol. 134, pp. 83-91, 2014.

[38] G. Arteel, R. Thurman, J. Yates, and J. Raleigh, "Evidence that hypoxia markers detect oxygen gradients in liver: pimonidazole and retrograde perfusion of rat liver," British journal of cancer, vol. 72, p. 889, 1995.

[39] K. Okuda, Y. Okabe, T. Kadonosono, T. Ueno, B. G. Youssif, S. Kizaka-Kondoh, and H. Nagasawa, "2-Nitroimidazole-tricarbocyanine conjugate as a near-infrared fluorescent probe for in vivo imaging of tumor hypoxia," Bioconjugate chemistry, vol. 23, pp. 324-329, 2012.

[40] F. M. Hamann, R. Brehm, J. Pauli, M. Grabolle, W. Frank, W. A. Kaiser, D. Fischer, U. Resch-Genger, and I. Hilger, "Controlled modulation of serum protein binding and biodistribution of asymmetric cyanine dyes by variation of the number of sulfonate groups," Molecular imaging, vol. 10, p. 7290.2011. 00005, 2011.

[41] A. J. Varghese, S. Gulyas, and J. K. Mohindra, "Hypoxia-dependent reduction of 1-(2-nitro-1-imidazolyl)-3-methoxy-2-propanol by Chinese hamster ovary cells and KHT tumor cells in vitro and in vivo," Cancer research, vol. 36, pp. 3761-3765, 1976.

[42] A. J. Franko, J. A. Raleigh, R. G. Sutherland, and K. J. Soderlind, "Metabolic binding of misonidazole to mouse tissues: comparison between labels on the ring and side chain, and the production of tritiated water," Biochemical pharmacology, vol. 38, pp. 665-670, 1989.

[43] I. Flockhart, P. Large, D. Troup, S. Malcolm, and T. Marten, "Pharmacokinetic and metabolic studies of the hypoxic cell radiosensitizer misonidazole," Xenobiotica, vol. 8, pp. 97-105, 1978.

[44] J. A. Raleigh and C. J. Koch, "Importance of thiols in the reductive binding of 2-nitroimidazoles to macromolecules," Biochemical pharmacology, vol. 40, pp. 2457-2464, 1990.

[45] J. Raleigh, A. Franko, E. Treiber, J. Lunt, and P. Allen, "Covalent binding of a fluorinated 2-nitroimidazole to EMT-6 tumors in Balb/C mice: detection by F-19 nuclear magnetic resonance at 2.35 T," International journal of radiation oncology, biology, physics, vol. 12, pp. 1243-1245, 1986.

[46] D. J. Van Os-Corby, C. J. Koch, and J. D. Chapman, "Is misonidazole binding to mouse tissues a measure of cellular pO2?," Biochemical pharmacology, vol. 36, pp. 3487-3494, 1987.

[47] J. Cline, D. Thrall, R. Page, A. Franko, and J. Raleigh, "Immunohistochemical detection of a hypoxia marker in spontaneous canine tumours," British journal of cancer, vol. 62, p. 925, 1990.

[48] G. Miller, J. Ngan-Lee, and J. Chapman, "Intracellular localization of radioactively labeled misonidazole in EMT-6 tumor cells in vitro," International Journal of Radiation Oncology* Biology* Physics, vol. 8, pp. 741-744, 1982.

[49] J. Raleigh, G. Miller, A. Franko, C. Koch, A. Fuciarelli, and D. Kelly, "Fluorescence immunohistochemical detection of hypoxic cells in spheroids and tumours," British journal of cancer, vol. 56, p. 395, 1987.

[50] G. E. Arteel, R. G. Thurman, and J. A. Raleigh, "Reductive metabolism of the hypoxia marker pimonidazole is regulated by oxygen tension independent of the pyridine nucleotide redox state," European Journal of Biochemistry, vol. 253, pp. 743-750, 1998.

[51] H. Jiang, N. V. Iftimia, Y. Xu, J. A. Eggert, L. L. Fajardo, and K. L. Klove, "Near-infrared optical imaging of the breast with model-based reconstruction," Academic radiology, vol. 9, pp. 186-194, 2002.

[52] R. Danen, Y. Wang, X. Li, W. Thayer, and A. Yodh, "Regional Imager for Low‐Resolution Functional Imaging of the Brain with Diffusing Near‐Infrared Light," Photochemistry and Photobiology, vol. 67, pp. 33-40, 1998.

[53] L.-Y. Chen, J.-M. Yu, M.-C. Pan, S.-Y. Sun, C.-C. Chou, and M.-C. Pan, "Comparisons of diffuse optical imaging between direct-current and amplitude-modulation instrumentations," Optical and Quantum Electronics, vol. 48, pp. 1-11, 2016.

[54] V. Ntziachristos, X. Ma, and B. Chance, "Time-correlated single photon counting imager for simultaneous magnetic resonance and near-infrared mammography," Review of Scientific Instruments, vol. 69, pp. 4221-4233, 1998.

[55] L. V. Wang and H.-i. Wu, Biomedical optics: principles and imaging: John Wiley & Sons, 2012.

[56] B. J. Tromberg, A. Cerussi, N. Shah, M. Compton, A. Durkin, D. Hsiang, J. Butler, and R. Mehta, "Imaging in breast cancer: diffuse optics in breast cancer: detecting tumors in pre-menopausal women and monitoring neoadjuvant chemotherapy," Breast Cancer Research, vol. 7, p. 1, 2005.

[57] R. Choe, S. D. Konecky, A. Corlu, K. Lee, T. Durduran, D. R. Busch, S. Pathak, B. J. Czerniecki, J. Tchou, and D. L. Fraker, "Differentiation of benign and malignant breast tumors by in-vivo three-dimensional parallel-plate diffuse optical tomography," Journal of biomedical optics, vol. 14, pp. 024020-024020-18, 2009.

[58] S. P. Poplack, T. D. Tosteson, W. A. Wells, B. W. Pogue, P. M. Meaney, A. Hartov, C. A. Kogel, S. K. Soho, J. J. Gibson, and K. D. Paulsen, "Electromagnetic breast imaging:

Results of a pilot study in women with abnormal mammograms 1," Radiology, vol. 243, pp. 350-359, 2007.

[59] X. Intes, "Time-domain optical mammography SoftScan: Initial Results1," Academic radiology, vol. 12, pp. 934-947, 2005.

[60] L. Spinelli, A. Torricelli, A. Pifferi, P. Taroni, G. Danesini, and R. Cubeddu, "Characterization of female breast lesions from multi-wavelength time-resolved optical mammography," Physics in medicine and biology, vol. 50, p. 2489, 2005.

[61] F. Collettini, J. Martin, F. Diekmann, E. Fallenberg, F. Engelken, S. Ponder, T. Kroencke, B. Hamm, and A. Poellinger, "Diagnostic performance of a Near-Infrared Breast Imaging system as adjunct to mammography versus X-ray mammography alone," European radiology, vol. 22, pp. 350-357, 2012.

[62] Q. Zhu, P. U. Hegde, A. Ricci Jr, M. Kane, E. B. Cronin, Y. Ardeshirpour, C. Xu, A. Aguirre, S. H. Kurtzman, and P. J. Deckers, "Early-Stage Invasive Breast Cancers: Potential Role of Optical Tomography with US Localization in Assisting Diagnosis 1," Radiology, vol. 256, pp. 367-378, 2010.

[63] Q. Zhu, P. A. DeFusco, A. Ricci Jr, E. B. Cronin, P. U. Hegde, M. Kane, B. Tavakoli, Y. Xu, J. Hart, and S. H. Tannenbaum, "Breast cancer: assessing response to neoadjuvant chemotherapy by using US-guided near-infrared tomography," Radiology, vol. 266, pp. 433-442, 2013.

[64] N. Shah, A. Cerussi, C. Eker, J. Espinoza, J. Butler, J. Fishkin, R. Hornung, and B. Tromberg, "Noninvasive functional optical spectroscopy of human breast tissue," Proceedings of the National Academy of Sciences, vol. 98, pp. 4420-4425, 2001.

[65] A. E. Cerussi, A. J. Berger, F. Bevilacqua, N. Shah, D. Jakubowski, J. Butler, R. F. Holcombe, and B. J. Tromberg, "Sources of absorption and scattering contrast for near-infrared optical mammography," Academic radiology, vol. 8, pp. 211-218, 2001.

[66] T. Svensson, J. Swartling, P. Taroni, A. Torricelli, P. Lindblom, C. Ingvar, and S. Andersson-Engels, "Characterization of normal breast tissue heterogeneity using time-resolved near-infrared spectroscopy," Physics in medicine and biology, vol. 50, p. 2559, 2005.

[67] W. Mo, T. S. Chan, L. Chen, and N. Chen, "Quantitative characterization of optical and physiological parameters in normal breasts using time-resolved spectroscopy: in vivo results of 19 Singapore women," Journal of biomedical optics, vol. 14, pp. 064004-064004-7, 2009.

[68] T. Yates, J. C. Hebden, A. Gibson, N. Everdell, S. R. Arridge, and M. Douek, "Optical tomography of the breast using a multi-channel time-resolved imager," Physics in medicine and biology, vol. 50, p. 2503, 2005.

[69] K. Suzuki, Y. Yamashita, K. Ohta, M. Kaneko, M. Yoshida, and B. Chance, "Quantitative measurement of optical parameters in normal breasts using time-resolved spectroscopy: in vivo results of 30 Japanese women," Journal of biomedical optics, vol. 1, pp. 330-334, 1996.

[70] T. Durduran, R. Choe, J. Culver, L. Zubkov, M. Holboke, J. Giammarco, B. Chance, and A. Yodh, "Bulk optical properties of healthy female breast tissue," Physics in medicine and biology, vol. 47, p. 2847, 2002.

[71] D. Grosenick, K. T. Moesta, H. Wabnitz, J. Mucke, C. Stroszczynski, R. Macdonald, P. M. Schlag, and H. Rinneberg, "Time-domain optical mammography: initial clinical results on detection and characterization of breast tumors," Applied optics, vol. 42, pp. 3170-3186, 2003.

[72] D. Grosenick, H. Wabnitz, K. T. Moesta, J. Mucke, P. M. Schlag, and H. Rinneberg, "Time-domain scanning optical mammography: II. Optical properties and tissue parameters of 87 carcinomas," Physics in medicine and biology, vol. 50, p. 2451, 2005.

[73] L. Spinelli, A. Torricelli, A. Pifferi, P. Taroni, G. M. Danesini, and R. Cubeddu, "Bulk optical properties and tissue components in the female breast from multiwavelength time-resolved optical mammography," Journal of biomedical optics, vol. 9, pp. 1137-1142, 2004.

[74] Q. Fang and D. A. Boas, "Monte Carlo simulation of photon migration in 3D turbid media accelerated by graphics processing units," Optics express, vol. 17, pp. 20178-20190, 2009.

[75] Q. Fang, J. Selb, S. A. Carp, G. Boverman, E. L. Miller, D. H. Brooks, R. H. Moore, D. B. Kopans, and D. A. Boas, "Combined optical and X-ray tomosynthesis breast imaging 1," Radiology, vol. 258, pp. 89-97, 2011.

[76] B. W. Pogue, S. P. Poplack, T. O. McBride, W. A. Wells, K. S. Osterman, U. L. Osterberg, and K. D. Paulsen, "Quantitative Hemoglobin Tomography with Diffuse Near-Infrared Spectroscopy: Pilot Results in the Breast 1," Radiology, vol. 218, pp. 261-266, 2001.

[77] A. Pifferi, P. Taroni, A. Torricelli, F. Messina, R. Cubeddu, and G. Danesini, "Four-wavelength time-resolved optical mammography in the 680 980-nm range," Optics letters, vol. 28, pp. 1138-1140, 2003.

[78] N. G. Chen, P. Guo, S. Yan, D. Piao, and Q. Zhu, "Simultaneous near-infrared diffusive light and ultrasound imaging," Applied optics, vol. 40, pp. 6367-6380, 2001.

[79] Q. Zhu, A. Ricci Jr, P. Hegde, M. Kane, E. Cronin, A. Merkulov, Y. Xu, B. Tavakoli, and S. Tannenbaum, "Assessment of Functional Differences in Malignant and Benign Breast Lesions and Improvement of Diagnostic Accuracy by Using US-guided Diffuse Optical Tomography in Conjunction with Conventional US," Radiology, p. 151097, 2016.

[80] Y. Ardeshirpour, M. Huang, and Q. Zhu, "Effect of the chest wall on breast lesion reconstruction," Journal of Biomedical Optics, vol. 14, pp. 044005-044005-14, 2009.

[81] C. Xu and Q. Zhu, "Estimation of chest-wall-induced diffused wave distortion with the assistance of ultrasound," Applied optics, vol. 44, pp. 4255-4264, 2005.

[82] M. Das, C. Xu, and Q. Zhu, "Analytical solution for light propagation in a two-layer tissue structure with a tilted interface for breast imaging," Applied optics, vol. 45, pp. 5027-5036, 2006.

[83] C. Xu, M. Das, Y. Ardeshirpour, and Q. Zhu, "Image reconstruction method for a two-layer tissue structure accounts for chest-wall effects in breast imaging," Journal of biomedical optics, vol. 13, pp. 064029-064029-13, 2008.

[84] Y. Xu and Q. Zhu, "Estimation and imaging of breast lesions using a two-layer tissue structure by ultrasound-guided optical tomography," Journal of Biomedical Optics, vol. 20, pp. 066002-066002, 2015.

[85] N. Yoshizawa, Y. Ueda, H. Nasu, H. Ogura, E. Ohmae, K. Yoshimoto, Y. Takehara, Y. Yamashita, and H. Sakahara, "Effect of the chest wall on the measurement of hemoglobin concentrations by near-infrared time-resolved spectroscopy in normal breast and cancer," Breast Cancer, pp. 1-7, 2015.

[86] F. Zhou, A. Mostafa, and Q. Zhu, "Improving breast cancer diagnosis by reducing chest wall effect in diffuse optical tomography," Journal of biomedical optics, vol. 22, pp. 036004-036004, 2017.

[87] C. Xu, H. Vavadi, A. Merkulov, H. Li, M. Erfanzadeh, A. Mostafa, Y. Gong, H. Salehi, S. Tannenbaum, and Q. Zhu, "Ultrasound-Guided Diffuse Optical Tomography for Predicting and Monitoring Neoadjuvant Chemotherapy of Breast Cancers Recent Progress," Ultrasonic imaging, p. 0161734615580280, 2015.

[88] J. H. Youk, E.-K. Kim, M. J. Kim, and K. K. Oh, "Imaging findings of chest wall lesions on breast sonography," Journal of Ultrasound in Medicine, vol. 27, pp. 125-138, 2008.

[89] A. Mostafa, H. Vavadi, and Q. Zhu, "Extraction of Tumor Features from Ultrasound Images for Diffused Optical Tomography Reconstruction," in Optical Tomography and Spectroscopy, 2016, p. JTu3A. 14.

[90] J. Revell, M. Mirmehdi, and D. McNally, "Applied review of ultrasound image feature extraction methods," in The 6th Medical Image Understanding and Analysis Conference, 2002, pp. 173-176.

[91] F. Zana and J.-C. Klein, "Segmentation of vessel-like patterns using mathematical morphology and curvature evaluation," IEEE transactions on image processing, vol. 10, pp. 1010-1019, 2001.

[92] B. S. Manjunath and W.-Y. Ma, "Texture features for browsing and retrieval of image data," IEEE Transactions on pattern analysis and machine intelligence, vol. 18, pp. 837-842, 1996.

[93] M. Haghighat, S. Zonouz, and M. Abdel-Mottaleb, "CloudID: trustworthy cloud-based and cross-enterprise biometric identification," Expert Systems with Applications, vol. 42, pp. 7905-7916, 2015.

[94] D. H. Ballard, "Generalizing the Hough transform to detect arbitrary shapes," Pattern recognition, vol. 13, pp. 111-122, 1981.

[95] J. Canny, "A computational approach to edge detection," IEEE Transactions on pattern analysis and machine intelligence, pp. 679-698, 1986.

[96] K. Hajian-Tilaki, "Receiver operating characteristic (ROC) curve analysis for medical diagnostic test evaluation," Caspian journal of internal medicine, vol. 4, p. 627, 2013.

[97] X. Robin, N. Turck, A. Hainard, N. Tiberti, F. Lisacek, J.-C. Sanchez, and M. Müller, "pROC: an open-source package for R and S+ to analyze and compare ROC curves," BMC bioinformatics, vol. 12, p. 1, 2011.

[98] E. Venkatraman and C. B. Begg, "A distribution-free procedure for comparing receiver operating characteristic curves from a paired experiment," Biometrika, vol. 83, pp. 835-848, 1996.

[99] N. Yoshizawa, Y. Ueda, H. Nasu, H. Ogura, E. Ohmae, K. Yoshimoto, Y. Takehara, Y. Yamashita, and H. Sakahara, "Effect of the chest wall on the measurement of hemoglobin concentrations by near-infrared time-resolved spectroscopy in normal breast and cancer," Breast Cancer, vol. 23, pp. 844-850, 2016.

[100] N. C. Biswal, Y. Xu, and Q. Zhu, "Imaging tumor oxyhemoglobin and deoxyhemoglobin concentrations with ultrasound-guided diffuse optical tomography," Technol Cancer Res Treat, vol. 10, pp. 417-29, Oct 2011.

[101] H. Jang, T. J. Pfefer, and Y. Chen, "Solid hemoglobin-polymer phantoms for evaluation of biophotonic systems," Opt Lett, vol. 40, pp. 4321-4, Sep 15 2015.

[102] K. D. Vandegriff and J. S. Olson, "The kinetics of O2 release by human red blood cells in the presence of external sodium dithionite," J Biol Chem, vol. 259, pp. 12609-18, Oct 25 1984.

[103] H. Jang, K. Singh, H.-W. Wang, T. Pfefer, and Y. Chen, "Oximetry system performance assessment with POM (acetal) phantoms incorporating hemoglobin calibration standards and customized saturation levels," in SPIE BiOS, 2015, pp. 931503-931503-7.

[104] http://chemed.chem.purdue.edu/genchem/topicreview/bp/1biochem/blood3.html

[105] http://sashpsg.blogspot.com/2015/02/photoplethysmography.html

Appendix I. Three generations of dye-conjugates and their molecular structures

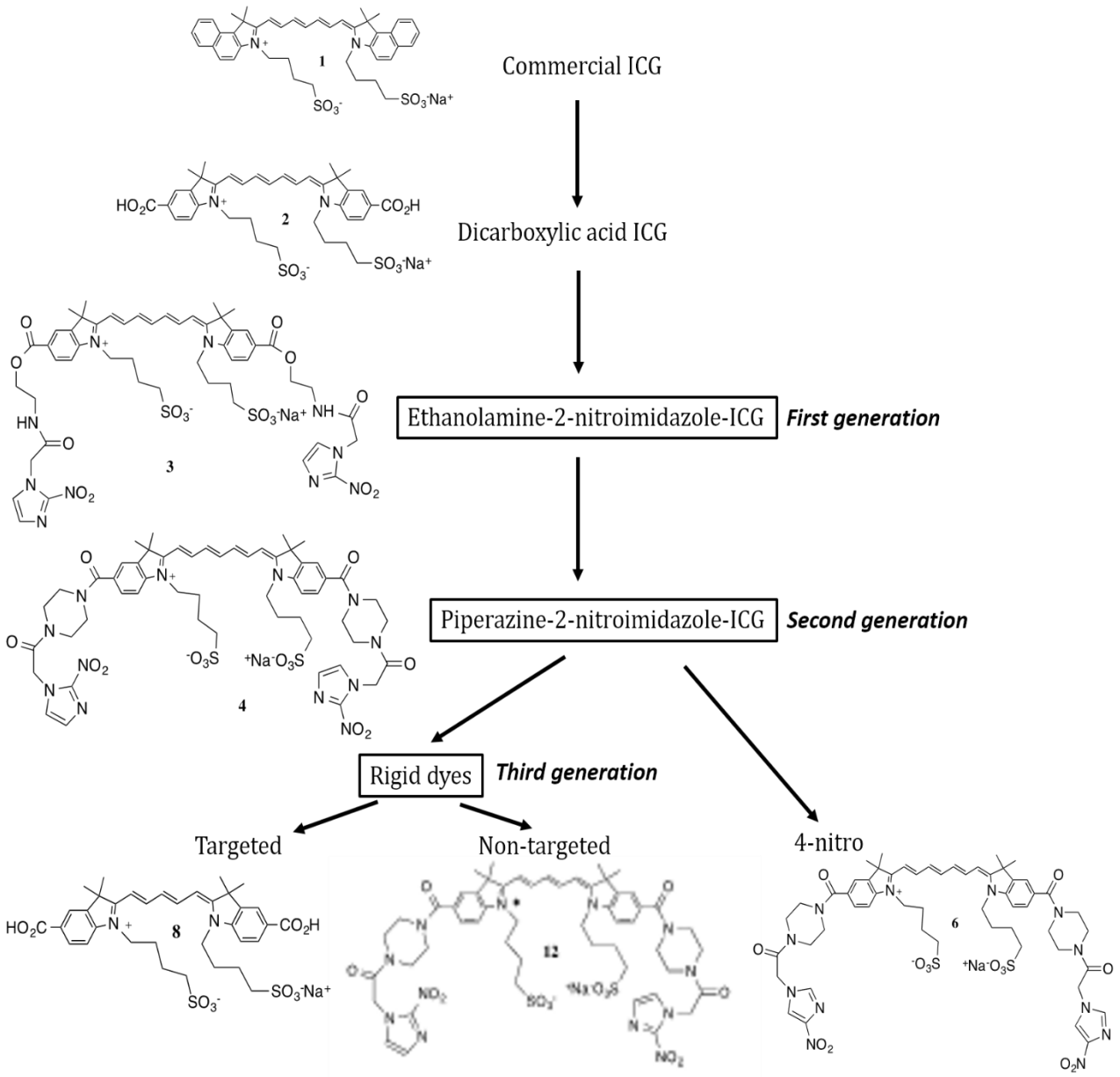

Appendix II. Procedures used for making solid breast tissue phantom

Materials: RTV silicone base, hardener, Titanium dioxide (TiO_2), Indian ink

Procedures:

1. Weigh 1 kg RTV silicone base;

2. Weigh 31 g hardener;

3. Weight 0.6 g TiO_2;

4. Get 5.5 µl Indian ink with pipette and dilute with 70 µl H_2O;

4. Add the TiO_2 and diluted Indian ink into hardener, and stir well with a mixer;

5. Sonicate the mixture for 10 min;

6. Stir again with the mixer;

6. Add the mixture into RTV silicone base and stir for 20 min;

7. Take 3 rounds of vacuuming and stirring procedures, each with 10 min;

8. Pour the mixture into a container and placed under vacuum overnight. It will become dry in the room temperature.

Appendix III. Hemoglobin concentration calculation

Suppose original hemoglobin solution concentration is:

$$tHb = 138 \text{ g/L}$$

For hemoglobin: (http://omlc.org/spectra/hemoglobin/)

$$MW \text{ (molecule weight)} = 64{,}500 \text{ g/mole}$$

So, the concentration in molar is:

$$c = 138 \text{ g/L} / 64{,}500 \text{ g/mole} = 2.1 \text{ mM}$$

The ampule has 1.7 ml hemoglobin solution. Suppose one can get 1.5 ml from it (it's hard to get all of them), then in order to prepare all the concentrations it can be diluted to:

$$180\ \mu M: V = 1.5 \text{ mL} \times 2.1 \text{ mM} / 180\ \mu M = 17.5 \text{ mL}$$

$$100\ \mu M: V = 1.5 \text{ mL} \times 2.1 \text{ mM} / 100\ \mu M = 31.5 \text{ mL}$$

The absorption coefficient (μ_a) can be calculated as (also referred to http://omlc.org/spectra/hemoglobin/) :

$$\mu_a(\lambda) = 2.303 \times \varepsilon(\lambda) \times c$$

For example, for 100 μM HbO_2 the absorption coefficient at 780 nm can be calculated:

$$\mu_a = 2.303 \times 710 \text{ /cm/M} \times 100 \times 10^{-6} \text{ M} = 0.164 \text{ / cm}$$

Appendix IV. Deoxy-Hb solution preparation procedures

The de-oxygenated hemoglobin (Hb) solution is prepared by adding $Na_2S_2O_4$ solution into the diluted oxygenated hemoglobin (HbO_2). Below are the procedures for making 180 μM HbO_2 and Hb solutions.

Materials: Human purified hemoglobin solution, purified water, $Na_2S_2O_4$, dry ice, glass ball, hot glue.

Procedures:

1. Dilute original solution with purified H_2O to solution **A**: 1.5 ml->15 ml;
2. Prepare 180 μM HbO_2 and Hb solutions
    - For HbO_2 solution, 3.5 ml solution **A** + 0.5 ml purified H_2O;
    - For Hb solution, 3.5 ml solution **A** + 0.5 ml purified H_2O with 50 mg $Na_2S_2O_4$;
    - For Hb solution, mix at temperature ~0 °C (on top of dry ice, when the solution is close to be frozen);
3. Fill the solution into 2 cm glass ball, and seal the ball quickly with hot glue;
4. Incubate at ~37 °C for 6 min;
5. Setup the ball and probe in intralipid and start to measure. Finish measurement in less than 10 min.

Notes:

1. For Hb measurement, make sure the intralipid is cold to 0-5 °C (can use dry ice);
2. As a calibration, the SO_2 of Hb solution measured by spectrometer decreased along 6 min incubation after adding $Na_2S_2O_4$. The values are listed below.

Time	1 min	2 min	3 min	4 min	5 min	6 min
SO2	9.7%	7.3%	7.3%	7.0%	6.4%	5.3%